Research Square

Preprints are preliminary reports that have not undergone peer review.
They should not be considered conclusive, used to inform clinical practice,
or referenced by the media as validated information.

Comparative performance analysis of direct-coupled DC and variable-frequency AC photovoltaic water pumping systems under tropical climatic conditions

Felix Ngangoum Welaji
Université de Yaoundé I
Ariel Teyou Ngoupo
Université de Yaoundé I
Bertrand Bodo
Université de Yaoundé I
/ Yaouba
Institut de Recherches Géologiques et Minières
Venant Sorel Chara-Dackou
chav7@yahoo.com

University of Bangui
Charles Bertrand Gubong Takam
Institut de Recherches Géologiques et Minières
Lyse Vanessa Ngansop
Institut de Recherches Géologiques et Minières
Antoine Fanyep Nana
Institut de Recherches Géologiques et Minières
Elie Bertrand Kegne Signe
Institut de Recherches Géologiques et Minières

Research Article

Keywords: Photovoltaic water pumping, Direct-coupled DC, Variable-frequency AC, Adaptive P&O MPPT, Site-specific assessment, Cameroon

Posted Date: October 30th, 2026

DOI: https://doi.org/10.21203/rs.3.rs-11267446/v1

License: This work is licensed under a Creative Commons Attribution 4.0 International License.
Read Full License

Additional Declarations: No competing interests reported.

Comparative performance analysis of direct-coupled DC and variable-frequency AC photovoltaic water pumping systems under tropical climatic conditions

Felix Ngangoum Welaji,[1,2] Ariel Teyou Ngoupo,[1,*], Bertrand Bodo[1], Yaouba[2], Venant Sorel Chara-Dackou[3,*], Charles Bertrand Gubong Takam[2], Lyse Vanessa Ngansop[2], Antoine Fanyep Nana[2], Elie Bertrand Kegne Signe[2]

[1]*University of Yaoundé I, Faculty of Science, Department of Physics, P.O. Box: 812, Yaoundé, Cameroon*
[2]*Research Centre for Renewable Energy, Institute of Geological and Mining Research, P.O. Box 4110, Yaoundé, Cameroon*
[3]*Carnot Energy Laboratory (CEL), Department of Physics, Faculty of Science, University of Bangui, P.O. Box 1450, Bangui, Central African Republic*

*Corresponding author: A. Teyou Ngoupo (arielteyou@yahoo.fr), V. S. Chara-Dackou (chav7@yahoo.com)

Abstract

Rural tropical areas often lack grid access and increasingly rely on photovoltaic water pumping. This study numerically compares two architectures under identical conditions (PV array, motor pump, hydraulic system, and demand): a direct-coupled DC system and a variable-frequency AC system with MPPT. Simulations use Typical Meteorological Year data (2005–2023) from four Cameroon sites, Meskine, Agola, Mbé, and Soa, at a 1-min time step. The PV generator is modeled with a single-diode model, the DC branch includes electromechanical motor dynamics, while the AC branch uses a quasi-steady power transfer model with an adaptive perturb-and-observe MPPT. Results show that the AC annual pumped volume exceeds DC at three sites: +18.9% at Meskine, +24.3% at Agola, and +7.8% at Mbé. At Soa, no AC gain was observed (−1.8%, not significant). This ranking follows the local climate and is mirrored in energy efficiency, temperature-corrected Performance Ratio, and operating time. Decomposing the AC gain shows that it stems mainly from better utilization of photovoltaic power through MPPT, which captures 84–87% of the theoretical potential at high-insolation sites versus 66% at Mbé, rather than from a faster restart response at the temporal resolution considered. AC superiority is therefore not universal but climate-dependent, which argues for a site-specific assessment before any technological choice is made. An explicit limitation of this study is that the irradiance time series, available hourly and then extrapolated to one-minute steps, cannot resolve sub-hourly transients.

Keywords: Photovoltaic water pumping; Direct-coupled DC; Variable-frequency AC; Adaptive P&O MPPT; Site-specific assessment; Cameroon

1. Introduction

Access to drinking water and irrigation water is a major challenge for remote rural areas in sub-Saharan Africa. Diesel-powered pumping systems are associated with high operating costs, a reliance on fossil fuels, and limited reliability in remote areas. The decline in the cost of photovoltaic modules has made solar photovoltaic water pumping systems (SPVWPS) increasingly competitive for these applications [1, 2]. These findings are consistent with those of previous reviews on renewable energy pumping systems, which document the continuous growth of research on the subject since the 1970s [3]. Two architectures dominate the literature: (a) DC systems, which power a DC motor (brushed or brushless, such as BLDC) without an intermediate conversion stage, and (b) AC systems, which convert the direct current produced by the panels into alternating current via an inverter to drive an induction motor. The dynamic comparison of these two architectures under variable irradiance sequences—characteristic of humid tropical regions—constitutes the central focus of this study. Humid tropical environments such as Cameroon and Central Africa are characterized by pronounced intraday variability in irradiance, particularly due to convective cloud cover. This variability provides a strong rationale for comparing architectures with differing conversion chains and electromechanical characteristics. However, our study uses irradiance data at one-minute (1 min) intervals; therefore, it does not allow for the quantification of sub-minute transients or irradiance drops occurring over a few seconds.

An SPVWPS may include a photovoltaic generator, a conversion and control stage, a motor-pump assembly, and, depending on the configuration, an intermediate storage device. In this study, the DC branch is directly coupled to the motor-pump assembly without an intermediate DC/DC converter, while the AC branch includes a DC/DC stage with MPPT followed by an inverter. The seminal review by Sontake and Kalamkar [1], which covers nearly 50 years of research on SPVWPS, classifies configurations according to motor type (brushed DC, BLDC, induction motor, PMSM), pump type (centrifugal, positive displacement, screw), and coupling topology. Subsequent reviews update and expand upon this classification, notably those by Li et al. [4], Gevorkov et al. [5] et Muralidhar et al. [6]. Meunier et al. [7] also propose an experimentally validated model of a photovoltaic pumping system designed for isolated rural communities, applicable to both DC and AC architectures.

The first generations of solar pumps relied almost exclusively on DC motors (separately excited, series, or shunt) coupled directly to the panels. The pioneering work by Metwally and Anis [8] modeled the dynamic behavior of a direct-coupled DC system, considering the magnetic saturation of the motor. Daud and Mahmoud [9] experimentally validated an induction motor system on a desert well. Fam and Balachander [10] are among the first to have studied the dynamics of a shunt DC motor powered by a photovoltaic array. Akbaba and Akbaba [11] studied the dynamics of a DC motor-pump system powered via a boost converter, while Mokeddem et al. [12] et Sontake et al. [13] experimentally characterized the seasonal performance variations of directly coupled DC systems.

The absence of a complex conversion stage allows for a nearly instantaneous response: as soon as irradiance increases after a cloud pass, the DC motor resumes rotation without any synchronization delay. This direct coupling reduces initial investment costs by eliminating the inverter, but the system has historically suffered from lower overall efficiency and significant pressure drops during irradiance transients, as well as a risk of unintended shutdowns and

restarts (ON/OFF cycles) under unstable sky conditions, which can lead to premature wear. In response to the need for larger-scale pumping, architectures using induction motors (AC) driven by a variable-frequency inverter have become the standard. Betka and Moussi [14] studied the performance optimization of a photovoltaic system with an induction motor. Chandel et al. [15] provide an overview of direct-coupled systems and their limitations compared to indirect architectures with inverters. AC motors are generally robust and well-suited for pumping applications requiring low maintenance, particularly when combined with a variable-frequency drive. The capacitive components of the inverter's DC bus can help mitigate certain rapid power fluctuations. On the other hand, the AC architecture includes several additional conversion stages, and its behavior during startup or restart depends on the control strategy and inverter settings. These characteristics must be distinguished from sub-minute phenomena, which are not quantitatively resolved by this simulation with 1-minute time steps.

The responsiveness of an SPVWPS to cloud cover depends heavily on the maximum power point tracking algorithm used. Conventional methods, such as Perturb & Observe (P&O) and Incremental Conductance (INC), have dynamic limitations: they struggle to converge quickly during a sudden drop in sunlight and generate oscillations around the MPP [16]. Arfaoui et al. [17] numerically evaluate the performance of a partially shaded pumping system using modern optimization techniques, illustrating the sensitivity of these algorithms to non-uniform irradiance conditions. More recent work documents hybrid and metaheuristic approaches. Ebrahim et al. [18] demonstrate that an MPPT controller based on PI/FOPI-type regulators, tested in real time on a "hardware-in-the-loop" test bench, significantly reduces power oscillations and improves dynamic response time compared to traditional controllers. Similarly, Saady et al. [19] demonstrate, through real-time simulation on dSPACE, that an MPPT based on artificial neural networks coupled with direct torque control improves the performance of an induction motor-driven pumping system. Vinoth and Singaravelu [20] compare P&O, fuzzy logic, and ANN on a high-power photovoltaic system and confirm the dynamic superiority of intelligent approaches under rapidly varying irradiance. From a more specifically electromechanical perspective, Bouchakour et al. [21] demonstrate, using a sliding-mode control applied to a buck-boost converter, that the architecture driven by an asynchronous motor achieves the best overall efficiency among three compared motor types (DC, asynchronous, and permanent-magnet synchronous). Elgendy et al. [22] had already established, for directly connected pumping systems, that constant-voltage control offers an attractive trade-off between simplicity and performance compared to conventional MPPT algorithms in certain operating ranges, a result that remains a fundamental reference for subsequent comparisons.

The physical characterization of cloud sequences is essential for evaluating the dynamic performance of SPVWPS. Neher et al. [23] analyzed 35 years of satellite data (SARAH-2.1) over West Africa and provide the most comprehensive reference available on irradiance variability in this tropical region. Mol et al. [24] reconcile observations of irradiance variability with cloud size distribution, providing a physical framework for modeling realistic irradiance "ramps" rather than idealized step-like drops. Agüera-Pérez et al. [25] present a review of the meteorological contexts associated with cloud-induced photovoltaic transients, including a taxonomy of variability regimes applicable to humid tropical climates. The literature shows that cloud passages can produce rapid and repeated variations in irradiance and that their effect on photovoltaic systems depends on the temporal scale considered [25, 24, 23]. These phenomena provide a rationale for studying the response of conversion chains and drives. However, in our

study, the quantitative analysis is limited to the available temporal resolution of 1 minute; characteristics on the order of a few seconds or sub-minute time scales are therefore not directly simulated. Table 1 summarizes, based on selected studies [14, 15, 9, 18, 8, 19, 20], the qualitative trends observed when comparing DC and AC architectures under rapidly varying irradiance. This is not a single experimental result but a synthesis of converging trends from several independent studies.

Table 1: *Qualitative summary of the comparative dynamic performance of DC and AC architectures under cloud sequences* [14, 15, 9, 18, 8, 19, 20].

Parameter	**DC (BLDC / brushed)**	**AC (induction + inverter)**
Start-up threshold	Low (≈Architecture-dependent)	Medium (≈Architecture-dependent)
Recovery after a cloud cover event	Almost instantaneous	Delayed (ramp imposed by the inverter)
Flow rate stability	More variable, sensitive to microvariations	More stable (inertia of the DC bus and the rotor)
Mechanical robustness / maintenance	Brushes/commutator: increased wear	Induction motor: robust, low maintenance
Risk during frequent cloud cover (30–60 s)	ON/OFF cycles, possible premature wear	Time lost during inverter restarts

DC-BLDC systems offer well-documented advantages in terms of efficiency and dynamic response speed, but suffer from frequent on/off cycles during periods of cloud cover. AC systems with variable-frequency drives provide better operational continuity during prolonged cloud cover, at the cost of higher control inertia during restart phases. Two optimization approaches recur frequently in recent literature: the use of predictive MPPT algorithms (fuzzy logic, neural networks) to keep the AC inverter in an "active standby" state rather than completely shut down [19, 20], and capacitive hybridization (adding supercapacitors to the DC bus) to maintain voltage during brief periods of cloud cover.

Wazed et al. [26] provide an overview of sustainable solar irrigation systems in sub-Saharan Africa and identify a recurring lack of studies on dynamic performance under real-world tropical conditions. Muhsen et al. [27] review the design methods and control strategies for SPVWPS, offering recommendations directly applicable to African contexts with abundant but unstable solar resources. In Cameroon, Nfah and Ngundam [28] studied the feasibility of hybrid pico-hydropower and photovoltaic systems for the electrification of remote villages, confirming the country's suitability as a case study for decentralized solar technologies. However, climate variability data specific to Central Africa remain scarcer in the literature than those available for West Africa or Southern Africa [23]. Focusing more specifically on photovoltaic pumping itself, several studies conducted in the Sudano-Sahelian region of Cameroon round out this overview. Deli et al. [29] modeled, using Matlab/Simulink, a photovoltaic pumping system combining a buck-boost converter and an incremental conductance (INC) MPPT algorithm, and then compared it to a direct-coupled system using irradiance and temperature data measured in the field in Maroua. Their annual simulations show

that MPPT optimization increases the monthly volume of water pumped from 12 - 43 m^3 (direct coupling) to 120-200 m^3 depending on the total head considered (24 to 60 m), confirming the value of incremental conductance for water supply in rural Sahelian areas. Building on this work, Deli et al. [30] developed and validated four semi-empirical models that predict, based on electrical power or irradiance measured on-site, the water flow rate of three actual photovoltaic pumping stations located in the Sahelian regions of Cameroon. The statistical evaluation of these models (mean bias, mean absolute error, mean squared error, and coefficient of determination) shows that a model incorporating the concept of a critical irradiance threshold ("solar radiation utilizability"), below which the motor pump cannot start, best reproduces the observed behavior, with coefficients of determination ranging from 0.95 to 0.97 for two of the three stations studied. Tchouli et al. [31] present a literature review dedicated to the optimization of photovoltaic pumping systems. This review lists the main pumping architectures (direct-coupled or with battery storage), common static converters (buck, boost, buck-boost, SEPIC, Cuk), DC and AC motors, as well as MPPT algorithms (P&O, INC, fuzzy logic) and air- or water-cooling techniques for photovoltaic generators. The authors note that the combined effect of temperature and irradiance is rarely studied simultaneously in the existing literature, and propose, as future directions, a variable-step hybrid INC algorithm coupled with fuzzy logic, as well as the cooling of panels mounted on solar trackers using the water being pumped—an approach directly applicable to the Cameroonian context.

Schmitter et al. [32] propose a framework for mapping the suitability of photovoltaic pumps for smallholder farmers in sub-Saharan Africa, while more recent work by Oppong Danso et al. [33] assesses the extent to which solar irrigation systems can naturally meet crop water needs in case studies across sub-Saharan Africa. Finally, Xie et al. [34] compare the costs of solar and diesel pumping for irrigation in sub-Saharan Africa, reinforcing the economic case for the solar systems examined in this review. From a technical and economic perspective, Tchudjo-Tchuente et al. [35] compare, based on field data collected at the PROLEG agro-industrial farm in Foumbot (Western Cameroon), the levelized cost of energy (LCOE) of a photovoltaic pumping system and that of a diesel generator used for drip irrigation of green beans. Based on actual system specifications (13.9 kWp peak photovoltaic power versus a 7.35 kW diesel generator), they arrive at an LCOE of 461.2 FCFA/kWh for solar versus 557.8 FCFA/kWh for diesel, with the break-even point reached as early as the fifth year of operation and a cumulative reduction of approximately 163,869 metric tons of CO_2 over 25 years in favor of solar power. This extends, at the level of a specific Cameroonian agricultural sector, the economic argument already put forward by Xie et al. [34] at the regional level.

A review of verified sources highlights several recurring gaps. First, comparisons between direct DC and AC architectures with comparable rated power, under the same solar resource and in the same tropical geographic context, remain relatively rare: most studies focus on a specific architecture [14, 15, 8]. Recent contributions from Cameroon confirm this trend: whether it concerns MPPT optimization of a direct-coupled DC string [29], models for predicting pumped flow rate [30], a review of optimization strategies for SPVWPS [31] or a techno-economic analysis comparing solar power with diesel [35], none of these studies directly compares, under the same solar resource, the dynamics of DC and AC architectures in response to cloud cover. Second, high-temporal-resolution solar variability data specific to Central Africa remain limited. Our study partially addresses these gaps through a homogeneous comparative across four sites in Cameroon, while explicitly maintaining the limitation imposed

by the 1-minute time step. It presents an annual comparison of DC and AC architectures based on representative meteorological profiles from Cameroon's four contrasting climate zones (Meskine, Agola, Mbé, and Soa), drawing on the models and experimental results of Bouchakour et al. [21] for the optimized control of the AC string, by Mokeddem et al. [12] or the characterization of direct DC coupling, and by Gunawan et al. [36] for the standardized test protocol (IEC 62253:2011) applied to single- and three-phase AC motors. The objective of our study is to evaluate and compare the technical and energy performance (energy and hydraulic performance) of DC-direct and AC photovoltaic pumping architectures in various tropical climates, with the aim of identifying the most suitable architecture based on climatic conditions and water needs. To this end, the study is organized as follows: Section 2 presents the four Cameroonian study sites (Meskine, Agola, Mbé, and Soa) and their climatic characteristics; Section 3 formalizes the mathematical equations governing the dynamic behavior of DC and AC systems; Section 4 describes the algorithm and flowchart of the simulation program developed in Fortran; Section 5 details the simulation methodology, the configurations compared, and the performance indicators; Section 6 presents and discusses the simulation results; finally, Section 7 concludes and proposes avenues for future research.

2. Overview of the study sites

The comparative study is based on four sites spread across Cameroon, selected for their representativeness of the country's main climate zones: Meskine (Far North Region, semi-arid Sahelian zone), Agola (Far North Region, Sudano-Sahelian zone), Mbé (Adamaoua Region, highlands), and Soa (Central Region, equatorial forest zone with high cloud cover). The Agola site originated from the experimental PV water pumping station described by Deli et al. [37] ; and the Meskine site refers to a vegetable-growing area [38]. Three distinct climate zones are thus represented: semi-arid Sahelian (Meskine), Sudano-Sahelian (Agola, Mbé), and equatorial forest (Soa). The geographical proximity of Meskine and Agola (≈ 120 km) allows for testing the reproducibility of the results at two sites within the same climate zone, while Mbé and Soa extend the analysis to wetter and cloudier conditions—in particular, to the frequency and intensity of cloud cover affecting the Central Region. Table 2 summarizes the geographic coordinates (WGS 84 system) and elevation of each site, while Table 3 presents the approximate distances between sites.

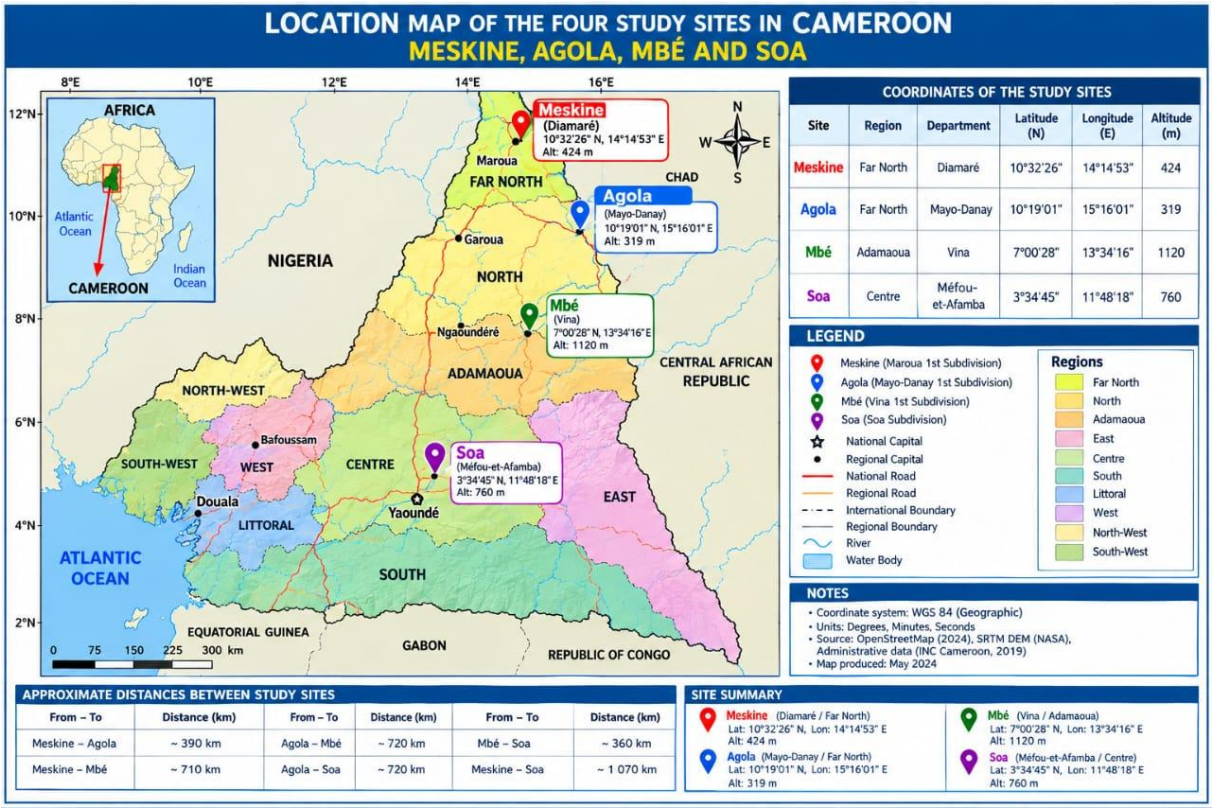


Figure 1 : *Map showing the locations of the four study sites in Cameroon: Meskine, Agola, Mbé, and Soa (base map: OpenStreetMap 2024; SRTM DTM, NASA; administrative data: INC Cameroon, 2019).*

Table 2: *Geographic coordinates of the study sites.*

Site	**Region/Department**	**Coordinates (Lat., Long.)**	**Elevation (m)**
Meskine	Far North/Diamaré	10°32’26" N, 14°14’53" E	424
Agola	Far North/Mayo-Danay	10°19’01" N, 15°16’01" E	319
Mbé	Adamaoua/Vina	7°00’28" N, 13°34’16" E	1,120
Soa	Center/Méfou-et-Afamba	3°34’45" N, 11°48’18" E	760

Table 3: *Approximate distances between study sites.*

Route	Meskine – Agola	Meskine – Mbé	Meskine – Soa	Agola – Mbé	Agola – Soa	Mbé – Soa
Distance (km)	≈ 120	≈ 400	≈ 820	≈ 400	≈ 900	≈ 430

Meskine (elevation 424 m) is representative of areas with high levels of sunshine but subject to a prolonged dry season and rare, brief but intense periods of cloud cover during the rainy season. Agola (319 m), located in the Sudano-Sahelian zone in the Far North, about 120 km from Meskine, has a climate similar to that of Meskine, with slight variations due to its more easterly location. Mbé (1,120 m), situated at a high elevation on the Adamaoua Highlands, experiences more frequent cloud cover due to the terrain. Soa (760 m), in the equatorial zone,

is characterized by a rapid alternation of sunny periods and cloudy spells, representing a comparatively cloudy climatic regime in the adopted dataset.

3. Implemented physical model

This section describes the equations solved by our simulation program. Both architectures share the same PV generator model, the same centrifugal pump law, and the same reservoir balance; they differ only in the conversion chain connecting the field to the pump shaft.

3.1. Photovoltaic generator

The photovoltaic module is represented by the one-diode, five-parameter model (photocurrent I_{ph}, reverse saturation current I_0, diode ideality factor n, series resistance R_S, shunt resistance R_{Sh}) [39], which is widely used for simulating PV systems. The current I delivered at the voltage V satisfies Equation (1).

$$I = I_{ph} - I_0 \left[exp\left(\frac{(V+I\cdot R_S)}{(N_c\cdot V_t)}\right) - 1\right] - \frac{(V+I\cdot R_S)}{R_{sh}} \quad (1)$$

Where N_c is the nuMbér of cells in series in the module and $V_t = (n \cdot k_B \cdot T_C)/q$ is the thermal voltage of the semiconductor. R_S and R_{Sh} are assumed to be constant.

The three parameters dependent on operating conditions are updated at each time step according to the standard relationships, given by Equation (2) [39, 40] :

$$\begin{cases} I_{ph} = I_{SC,STC} \cdot (G/G_{STC}) \cdot \left[1 + \alpha_{I_{SC}}(T_C - T_{STC})\right] \\ V_{OC}(T_C) = V_{OC,STC} \cdot \left[1 + \beta_{V_{OC}}(T_C - T_{STC})\right] \\ I_0 = \left(I_{SC,STC} - V_{OC}/R_{sh}\right)/\{exp[V_{OC}/(N_c \cdot V_t)] - 1\} \end{cases} \quad (2)$$

where $\alpha_{I_{SC}}$ and $\beta_{V_{OC}}$ are the manufacturer's temperature coefficients, the nuMbér of cells in series in the module, and $V_t = (n \cdot k_B \cdot T_C)/q$ is the thermal voltage of the semiconductor.

Equation (1) is solved using the Newton-Raphson method, initialized at $I = I_{ph}$, with a convergence criterion of 10^{-6} A and a maximum of 50 iterations; the argument of the exponential function is bounded to prevent numerical overflow during transients. The cell temperature is estimated from the ambient temperature and the irradiance in the module plane according to the NOCT model, given by Equation 3 [40, 41].

$$T_C = T_{amb} + \frac{G\cdot(NOCT-20)}{800} \quad (3)$$

The array consists of N_S modules in series and N_P strings in parallel. The configuration given by Equation 4, is assumed to be ideal (identical modules, no mismatch or partial shading).

$$I_{champ}(V_{champ}) = N_P \cdot I(V_{champ}/N_S) \quad (4)$$

3.2. Direct-Coupled DC Architecture

In each architecture, the PV array directly powers the armature of a separately excited DC motor that drives the pump: no converter, control unit, or tracking device is interposed. The operating point therefore results solely from the intersection of the field's I-V characteristic and the motor's electromechanical characteristic [8, 10].

The electrical time constant of the armature ($\tau_e = L_a/R_a$, on the order of a few milliseconds) is shorter than the meteorological time step; therefore, the armature dynamics are treated in a quasi-steady-state regime, and only the mechanical dynamics are integrated. The armature current i_a, with velocity ω, satisfies the implicit equation (5), which is solved by dichotomy on the interval $[0, 3I_{SC}]$. The angular velocity is obtained by integrating the mechanical equation (Equation 6) [8], since the resistance torque of a centrifugal pump is proportional to the square of the velocity ($T_r = K_P \cdot \omega^2$).

$$i_a = I_{champ}(R_a \cdot i_a + K_E \cdot \omega) \quad (5)$$

$$J \cdot \left(\frac{d\omega}{dt}\right) = K_T \cdot i_a - K_P \cdot \omega^2 \quad (6)$$

Where R_a is the armature resistance; L_a is the armature inductance; K_E is the emf constant; K_P is the torque constant; K_T is the electromagnetic constant; ω is the angular velocity of the motor.

Equation (6) is integrated using a fourth-order Runge-Kutta (RK4) scheme with a 1-ms time step, with irradiance and temperature held constant over the meteorological time step. Integration continues until the system stabilizes, with a deviation of less than 0.01 A and 0.01 rad/s between two successive moving averages over 100 steps, or for a maximum of 60 s of physical time. The electromagnetic torque and emf are related to the current and speed by $T_e = K_T \cdot i_a$ and $E = K_E \cdot \omega$, where $K_E = K_T$.

The electromechanical parameters are identified from the motor's nameplate (rated power $P_{nom} = 1.5\ kW$, rated voltage $V_{nom} = 120\ V$, rated current $I_{nom} = 12.5\ A$, rated speed $N_{nom} = 3000\ tr/min$, $\eta_{nom} = 0.85$) according to the standard procedure, given by Equation (7) [12].

$$\begin{cases} K_E = K_T = (\eta_{nom} \cdot V_{nom})/\omega_{nom} \ ; \ R_a = (V_{nom} - K_E \cdot \omega_{nom})/I_{nom} \\ J = (\tau_m \cdot T_{nom})/\omega_{nom} \ ; \ K_P = T_{nom}/\omega_{nom}^2 \end{cases} \quad (7)$$

Where $T_{nom} = (\eta_{nom} \cdot V_{nom} \cdot I_{nom})/\omega_{nom}$ and τ_m is the mechanical time constant. The set of parameters obtained is verified at the nominal point (reconstruction of V_{nom} to within ±1 V) before the simulation is launched. The numerical values are given in Table S3 (Supplementatry materials).

3.3. AC Architecture with a Frequency Converter

The AC branch is analyzed under quasi-steady-state conditions and represented by a power transfer model. This choice, discussed in Section 5.3, assumes that the internal dynamics of the conversion chain are fast relative to the 1-minute time step and that they introduce neither a restart delay nor an acceleration ramp at this time scale.

The tracking stage adjusts the field operating voltage using a P&O algorithm with an adaptive step size [16, 42] on the P-V characteristic. At each time step, the local slope is evaluated using a 1% probe perturbation, given by Equation (8).

$$\frac{\partial P}{\partial V} \approx \frac{[P(V+\delta V) - P(V)]}{\delta V}, \text{ where } \delta V = 0{,}01 \times V \quad (8)$$

The maximum power point is characterized by the vanishing of this derivative. The setpoint voltage is then shifted by a step whose amplitude increases with the instantaneous field

power, in order to balance tracking accuracy at low irradiance with responsiveness at high power: It is given Equation (9).

$$\Delta V = \Delta V_{min} + (\Delta V_{max} - \Delta V_{min}) \cdot min\left(P/P_{réf}\,, 1\right) \quad (9)$$

$$V(k+1) = V(k) + sgn(\partial P/\partial V) \cdot \Delta V, \text{ bounded by } \left[0.1\,;\, 1.1 \cdot N_S \cdot V_{OC,STC}\right] \quad (10)$$

Only one iteration is performed per meteorological step, which limits the setpoint's rate of change to ΔV_{max} per minute; the scope of this assumption is examined in Section 5.3. The power drawn from the field is then transmitted to the pump shaft through a constant-efficiency drive η_{ond}, following the approach of Bouchakour et al. [21] with a minimum activation threshold of P_{seuil} and a cap set at the motor-pump unit's rated power, as the variable-speed drive does not allow the rated speed to be exceeded. It is given by Equation (11).

$$\begin{cases} P_{champ} = min(P_{MPP}, P_{nom}/\eta_{ond}) \\ P_{mot} = \eta_{ond} \cdot P_{champ} \;\; si\; P_{champ} \geq P_{seuil}, \;\; 0\; sinon \end{cases} \quad (11)$$

Beyond P_{nom}/η_{ond}, the available PV power is therefore not drawn. The rotational speed is derived from the mechanical power using the cubic affinity law for centrifugal pumps [43], with the motor efficiency, which is identical in both branches, simplifying to the power ratio (Equation 12).

$$\frac{\omega}{\omega_{nom}} = \left(\frac{P_{mot}}{P_{nom}}\right)^{1/3} \quad (12)$$

3.4. Centrifugal pump and hydraulic System

Both architectures drive a centrifugal pump with identical characteristics. The head is described by the affinity law [43], approximating the pump's characteristic curve with a flat curve over the useful flow rate range (Equation 13).

$$H_p(\omega) = H_{nom} \cdot (\omega/\omega_{nom})^2, \quad \text{where} \quad \omega/\omega_{nom} \leq 1 \quad (13)$$

The hydraulic network curve combines the static head of the well and quadratic pressure losses, in accordance with the classical formulation (Equation 14) [44].

$$H_{res}(Q) = H_{stat} + \Delta H_{nom} \cdot (Q/Q_{nom})^2 \quad (14)$$

The operating point is the intersection of (13) and (14), which directly yields the flow rate without iterative solution (Equation 15).

$$Q = \begin{cases} Q_{nom} \cdot \sqrt{\left[\frac{(H_{nom} \cdot (\omega/\omega_{nom})^2 - H_{stat})}{\Delta H_{nom}}\right]} \;\; if\; H_p(\omega) > H_{stat}\; and\; P \geq P_{dém} \\ 0 \qquad\qquad else \end{cases} \quad (15)$$

This formulation ensures that no flow is produced as long as the available head does not exceed the static head, in accordance with the actual behavior of a centrifugal pump, and that the flow rate remains bounded by the nominal flow rate. With the selected values ($H_{nom} = 40\; m, H_{stat} = 38\; m, \Delta H_{nom} = 2\; m$),), the flow rate is zero below 97.5% of the rated speed and reaches Q_{nom} at the rated speed; the implications of this narrow operating range are discussed in Section 5.3. At the operating point, the total head satisfies $HMT = H_p(\omega)$, and the useful hydraulic power is given by Equation 16.

$$P_{hyd} = \rho \cdot g \cdot Q \cdot HMT \quad (16)$$

3.5. Storage tank and operating filter

Storage is exclusively hydraulic: no battery is modeled. The reservoir volume is updated at each step using a simple balance equation bounded between zero and the capacity, identical to that used by Hadj Arab et al. [45], at Equation 17.

$$V = min\left\{V_{cap}, max\left[0, V(t) + \left(Q_{pompe}(t) - Q_{conso}(t)\right) \cdot \Delta t\right]\right\} \quad (17)$$

Where V is the volume of water in the reservoir (m^3), Q_{pompe} is the pumped flow rate (m^3/s), Q_{conso} is the consumption flow rate (m^3/s), Δt is the time step (s), and V_{cap} is the maximum reservoir capacity (m^3).

Overflow is calculated as $max\left[0, V_{tent} - V_{cap}\right]$ and the instantaneous deficit as $max[0, -V_{tent}]$, where is the volume before clipping. The consumption flow rate Q_{conso} remains constant over a 24-hour period.

Motor start counts are based on a filtered operating state, not on the instantaneous flow rate: a start is only validated after two consecutive minutes of non-zero flow, and a stop only after three consecutive minutes with no flow. This hysteresis filter simulates the time delay of real-world controllers and prevents minute-by-minute fluctuations around the flow threshold during cloudy periods from being counted as motor cycles. It affects only the cycle count; the physical flow rate, and thus the hydraulic and energy balances, remain unchanged.

3.6. Performance indicators

To ensure that the comparison of the two architectures covers the entire conversion chain, the instantaneous overall efficiency, calculated according to the IEC 62253:2011 standard [46], is expressed in both cases as a ratio of the power drawn from the PV array, with the inverter losses thus being attributed to the AC branch (Equation 18).

$$\eta_{inst} = P_{hyd}/P_{PV} = (\rho \cdot g \cdot Q \cdot HMT)/(V_{PV} \cdot I_{PV}) \quad (18)$$

For the annual analysis, the energy-weighted efficiency is used by Equation (19).

$$\eta_{ann} = \frac{E_{hyd}}{E_{PV}} = \frac{\sum_t P_{hyd}(t) \cdot \Delta t}{\sum_t P_{PV}(t) \cdot \Delta t} \quad (19)$$

The performance ratio is defined here in its electrical sense (IEC 61724-1 standard) as the ratio of the electrical energy actually generated to the energy that would be generated under STC conditions for the same incident irradiance (Equation 20) [47].

$$PR = \frac{E_{PV}}{G_{tot} \cdot A_{tot} \cdot \eta_{STC}} \quad (20)$$

Where G_{tot} is the cumulative irradiance in the plane of the modules [kWh/m^2], A_{tot} is the total area of the array, and η_{STC} is the module efficiency under STC conditions. This indicator does not include the hydraulic system. Unlike the PR of a grid-connected system, it is not an indicator of the generator's health: the power drawn here is dictated by the load, outside the maximum power point for the DC branch and limited to the generator set's rated power for the AC branch. It should therefore be interpreted as a field utilization rate, and differences between system

architectures primarily reflect a mismatch between the field and the motor-pump. The temperature-corrected PR (Equation 21) neutralizes the thermal effect according to the approach by Marion et al. [47] ; the temperature coefficient (α) of the maximum power used is that of crystalline silicon, whose typical value is 0.35–0.45%/°C [41]. This indicator allows for cross-site comparisons.

$$PR_T = \frac{PR}{1+\alpha\cdot(T_{cell}-25)} \quad (21)$$

Where α is the temperature coefficient of the maximum power and T_{cell} is the irradiance-weighted average cell temperature.

4. Algorithm used and corresponding flowchart

To compare DC and AC architectures under strictly identical conditions, a dedicated simulation program (pompage_pv_simulation, developed in Fortran) was used. It reproduces, at one-minute time steps over a full year, the behavior of the two architectures fed by the same meteorological profile (irradiance, ambient temperature), based on an electrical model of a photovoltaic generator with one diode and five parameters. The code is structured into thirteen independent modules, summarized in Table S1 (Supplementary Materials).

4.1. General flowchart of the program

Figure 2 shows the overall flow of the program, from initialization to writing the results. After initializing the constants and sizing the engine, the meteorological irradiance file is read to determine the nuMbér of time steps and days to be simulated. The time loop is the core of the program: at each step, the two architectures (DC and AC) are calculated in parallel, and their results are accumulated. Once the loop is complete, a series of post-processing modules calculates the aging, cost savings, carbon footprint, and reliability assessments before writing approximately fifteen result files.

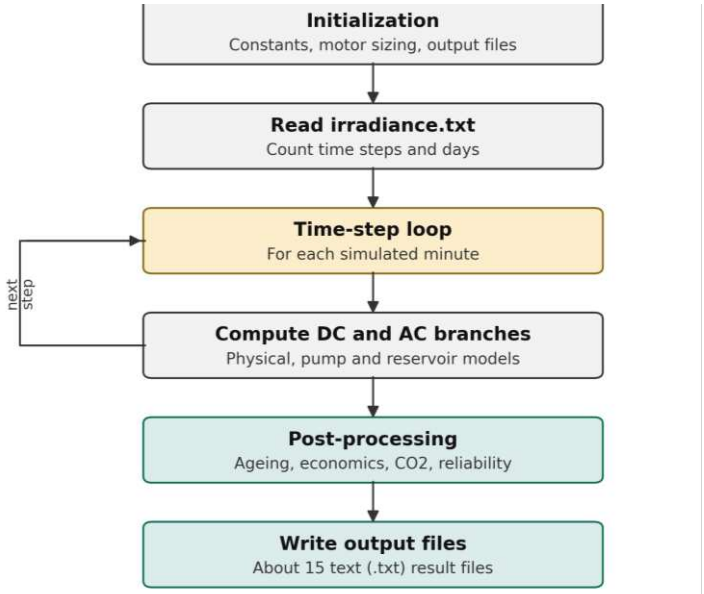


Figure 2: *General flowchart of the simulation program.*

4.2. Details of the calculation at each time step

Figure 3 details the operations performed at each time step for both branches. On the DC side, the armature current and the motor's angular velocity are integrated using the fourth-order Runge-Kutta method until convergence, which reflects the direct electromechanical coupling between the PV array and the motor, without a control stage. On the AC side, an adaptive-step MPPT algorithm searches for the field's maximum power point; the power is then transmitted through a fixed-efficiency inverter, capped at the drive's rated power. In both cases, the water flow rate is determined by a centrifugal pump law (the intersection of the pump curve and the hydraulic network curve); the reservoir is updated; and motor starts are counted using an anti-bounce hysteresis filter before the results of the time step are written to disk.

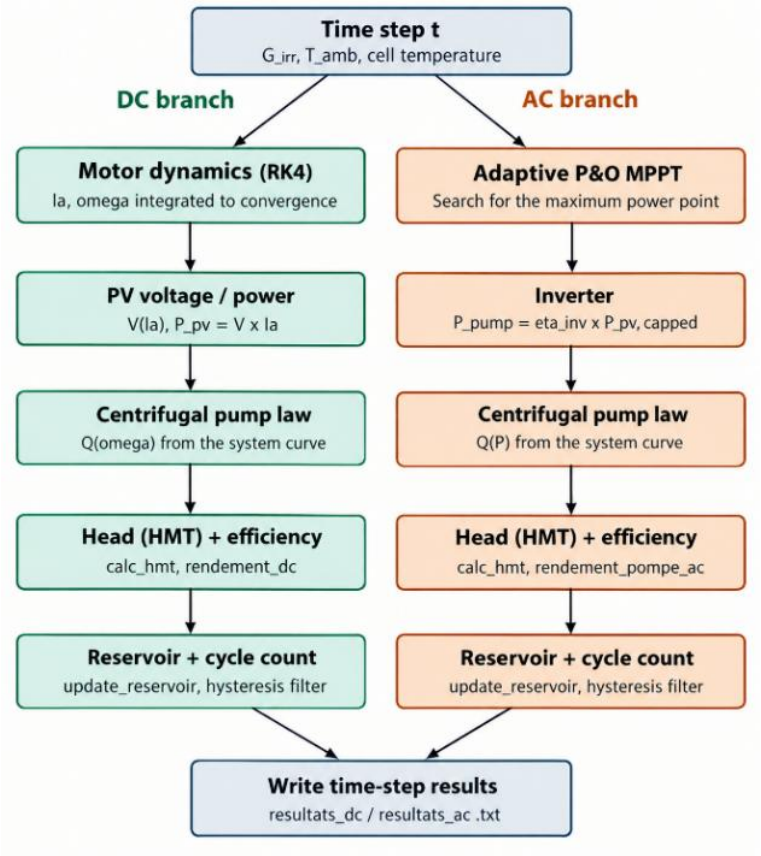


Figure 3: *Details of a time step calculation: DC and AC branches.*

4.3. Implemented physical models

The simulation program is structured into independent modules (Table S1, Supplementary Materials), the main ones of which are described below.

The mod_pv module implements a model with one diode and five parameters (I_{ph}, I_0, n, R_S, R_{Sh}), solved using the Newton-Raphson method to obtain the field current at a given voltage; the cell temperature is estimated based on the ambient temperature and irradiance according to the NOCT model.

The mod_dimensionnement_moteur module determines the electromechanical parameters of the DC motor (armature resistance R_a, inductance $L_a = L_m$, torque constant K_T, inertia J_m, quadratic friction coefficient K_p) based on its nameplate. The procedure is based on the standard equations for separately excited DC machines, assuming a nominal efficiency of 85%. The conversion parameters, efficiencies, and thresholds used for both architectures are summarized in Table S3 (Supplementary Materials).

The mod_dynamique module solves the differential equation for direct panel-motor coupling (Equation 6), where the quadratic resistance torque represents the hydraulic load of a centrifugal pump. This equation is integrated using a fourth-order Runge-Kutta (RK4) scheme until the system stabilizes at each 1-minute time step. Within the adopted modeling framework, the DC architecture is represented by an explicit electromechanical transient model, whereas the AC drive is treated quasi-statically.

The mod_mppt module implements an adaptive-step P&O algorithm (Equations 8–10), in which the voltage disturbance amplitude varies with the instantane al power of the field, in order to balance convergence speed and stability around the maximum power point.

The mod_pompe module determines the water flow rate based on the intersection between the pump's characteristic curve (head proportional to the square of the relative velocity) and the hydraulic network curve (static head plus quadratic pressure losses); this formulation ensures that no flow is produced as long as the available head does not exceed the static head of the well, in accordance with the actual behavior of a centrifugal pump.

The mod_hydraulique module calculates the total manometric head (HMT) as a function of flow rate (Equation 13), updates the reservoir volume at each time step (Equation 17), and evaluates the useful hydraulic power (Equation 16). The reservoir update is based on a simple water balance: the volume at the next time step is equal to the volume at the previous time step, plus the pumped flow rate and minus the consumption flow rate, with the result bounded between 0 and the maximum reservoir capacity.

Finally, the mod_controle module filters the pump's operating status to prevent overcounting of motor starts during cloudy periods: a start is validated only after two consecutive minutes of sustained flow, and a stop only after three consecutive minutes without flow. This anti-bounce hysteresis filter simulates the time delay inherent in actual controllers (AC drive, DC controller).

The two branches are not modeled at the same dynamic level. The DC branch is integrated using the RK4 method until convergence at each time step (start-up and acceleration transients are shown). The AC branch is treated in a quasi-steady-state regime. The photovoltaic electrical submodel (single-diode model) was validated against experimental I–V/P–V characteristics (Figure 4) derived from the manufacturer's data for the Suniva OPT270-60-4-100 module (Table S2, Supplementary materials). Table 4 shows deviations of less than 1.7% across all parameters (I_{SC}, V_{OC}, I_{MPP}, V_{MPP}, P_{max}), confirming the model's accuracy for the simulations. The error is calculated using Equation (22).

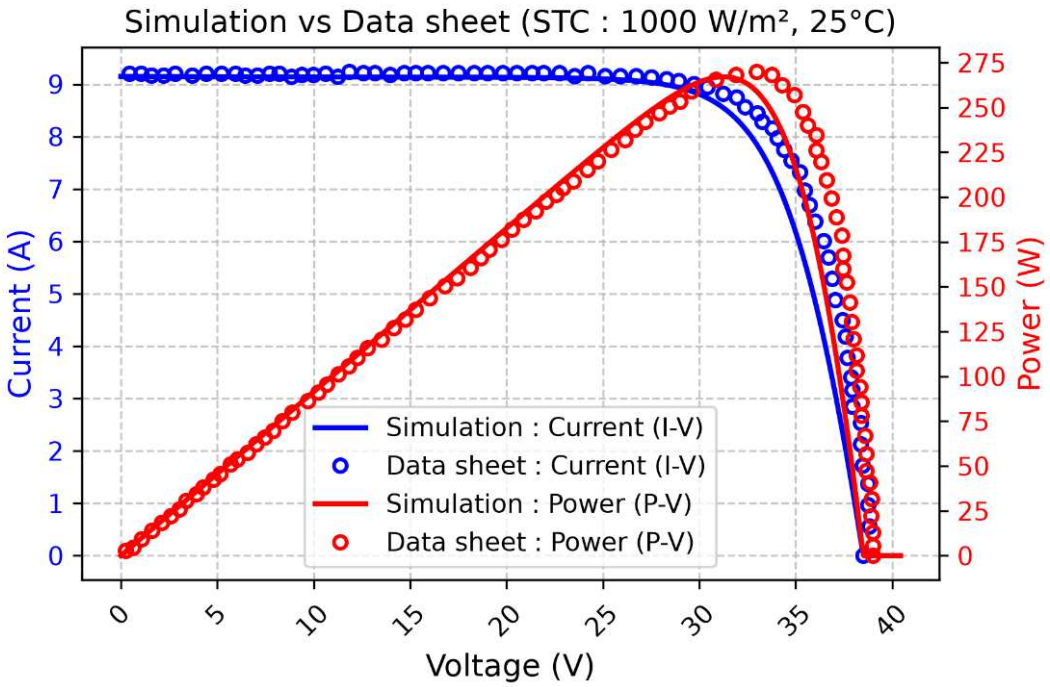


Figure 4: *Validation of the single-diode model: comparison of simulated and manufacturer-specified I-V and P-V curves under STC conditions (1000 W/m², 25 °C).*

Table 4: *Comparison of electrical parameters from the manufacturer's data sheet and those simulated under STC conditions (1000 W/m², 25 °C).*

Parameter	Data sheet	Simulation	Error (%)
I_{SC} (A)	9.15	9.15	0.00
V_{OC} (V)	38.50	38.50	0.00
I_{MPP} (A)	8.68	8.54	-1.61
V_{MPP} (V)	31.20	31.28	+0.26
P_{max} (W)	270.82	267.2	-1.34

$$\boldsymbol{Error}\ (\%) = \left(\frac{\boldsymbol{Simulation - Data\ sheet}}{\boldsymbol{Data\ sheet}}\right) \times \mathbf{100} \qquad (22)$$

The modeling choices adopted in the program are based, in particular, on the following works: the dynamics of direct PV-DC motor coupling [8], the design and control of photovoltaic pumping [27, 48], permissible duty cycles and starting conditions for rotating electrical machines (IEC 60034-1:2026 standard) [49], degradation of crystalline silicon in tropical climates [50, 51, 52, 53, 54, 55, 56], the affinity laws for centrifugal pumps [43], and a review of MPPT methods [42].

4.4. Post-processing modules

At the end of the annual time loop, several analysis modules process the accumulated results (Table S1):

- mod_postprocessing performs statistical sorting and selection of representative days used for the analysis of daily dynamics (Subsection 6.7.1). The selection is based on a percentile criterion (95^e, 50^e and 5^e) applied to the average daily irradiance;

- mod_fiabilite provides the hydraulic parameters used for the analysis of availability and production shortfall (Subsection 6.7.2), including the probability of water supply disruption (LWSP), the cumulative shortfall, and resilience indicators.

Other modules include mod_aging (electrical degradation of the PV array and replacement schedule), mod_economics (capital expenditure (CAPEX), operating expenses (OPEX), and levelized cost of water (LCOW)), and mod_carbon_footprint (life-cycle carbon footprint), are also implemented within the same simulation framework. In accordance with the limited scope of this study (technical and hydraulic comparison of DC and AC architectures), the detailed results of these analyses are not presented here and will be the subject of future work.

5. Methodology

5.1. Configurations compared

Two photovoltaic pumping configurations (Figure S1) are compared at each of the four sites presented in Section 2: (i) a DC system consisting of a photovoltaic array directly coupled to a DC motor driving a centrifugal pump, and (ii) an AC system consisting of the same photovoltaic array, a maximum power point tracking stage (Equations 8–10), and a constant-efficiency frequency converter (Equation 11) modeled using a quasi-steady-state power transfer model, driving a centrifugal pump with equivalent hydraulic characteristics. This modeling choice does not explicitly represent the internal control of an asynchronous machine; it assumes that its dynamics are fast relative to the 1-minute time step. Both systems are sized for the same peak power to ensure a comparison under equal solar resource conditions, in accordance with the approach adopted by Bouchakour et al. [21].

To ensure that any observed difference in performance between study sites can be unambiguously attributed to climate, all system parameters (Table 5) are kept strictly identical across sites, with the exception of climatic factors (irradiance, temperature). The consumption rate is set at 49 m^3/day (≈ 2 m^3/h) (Methodological Note A, Supplementary materials), which represents approximately 25% of the motor pump's rated flow rate (8 m^3/h). This sizing corresponds to the irrigation needs of a small agricultural plot and ensures that the pump operates at partial load, which is compatible with a 50 m^3 storage tank, providing a supply capacity of approximately one day's demand.

Table 5: *Common parameters imposed on both architectures to ensure a controlled comparison.*

Parameter	DC or AC configuration
PV Array Configuration	4 modules in series × 3 strings in parallel
PV peak power (kWp)	3.25
Reference module	Suniva OPT270-60-4-100
Tilt (°)	15
Azimuth (°)	0 (due south)
Static head (m)	38
Nominal head (m)	40
Nominal flow rate (m^3/h)	8

Tank volume (m^3)	50
Daily water demand (m^3/day)	49
Meteorological input	TMY file
Simulation time step (min)	1
Simulation duration (years)	1

5.2. Climate data and cloud cover sequences

The input meteorological time series were constructed from a Typical Meteorological Year (TMY) file generated for the coordinates of each site, covering the period 2005–2023 (source: PVGIS). The TMY provides hourly values for ambient temperature, relative humidity, wind speed and direction, atmospheric pressure, and irradiance components (horizontal global, direct normal, horizontal diffuse). Two distinct processing steps were applied to obtain time series with a one-minute (1 min) resolution:

- Non-radiative variables (temperature, humidity, wind, pressure) were linearly interpolated over time, from hourly resolution to minute resolution;
- The irradiance components were held constant within each hour (forward fill) and then projected onto the 15°-inclined plane at 1-minute intervals using the Hay-Davies anisotropic sky model, with a ground albedo of 0.2 and an azimuth of 0° (due south).

This procedure yields an apparent resolution of 1 minute, which does not capture sub-hourly irradiance fluctuations: the intra-hourly variability of irradiance is reconstructed by solar geometry, not by high-frequency measurements. This limitation is explicitly acknowledged and discussed in Section 5.3.

5.3. Scope of modeling, validation, and limitations

What has been validated. The electrical submodel of the PV generator was compared with the I-V and P-V characteristics from the technical data sheet for the Suniva OPT270-60-4-100 module under STC conditions (Figure 4, Table 4): the deviations remain below 1.7%. This verification focuses on reproducing a manufacturer's characteristic and confirms the model's single-diode configuration.

What has not been validated. No experimental measurements accompany the electromechanical, hydraulic, and conversion submodels. The motor parameters (Equation 7) are identified from the nameplate, without locked-rotor or no-load tests: they are consistent at the rated point but have not been validated outside of that point. Experimental studies in the literature [12, 36] and the IEC 62253:2011 standard [46] are used as methodological references for defining performance metrics and measurement procedures.

Asymmetry in the levels of description. The DC branch incorporates the mechanical transient of the motor-pump unit (Equation 6); the AC branch is quasi-steady-state, with neither a restart delay nor an acceleration ramp. This asymmetry favors the AC architecture: the reported deviations therefore constitute an upper bound on the gain, and the origin of this gain, whether due to MPP tracking or dynamics, cannot be distinguished.

MPPT Resolution. The tracker performs one iteration per step, i.e., a displacement limited to ΔV_{max} per minute (Equations 9–10), several orders of magnitude lower than that of

a real controller, but with a slope evaluated exactly. The tracking rate reported in this work is indicative and not representative of any particular physical algorithm.

Pump characteristics. The flat curve used (Equation 13) and the low head losses (2 m for 38 m of static head) limit the useful range to 97.5–100% of the nominal speed, which tends to amplify the simulated sensitivity of the flow rate to power deviations.

Temporal resolution of solar resources. The hourly components of the TMY are held constant and then projected to the minute using the Hay-Davies model [57]: sub-hourly variability is represented only to the extent that it is already contained in the hourly values. This is the main limitation of this study; it influences the interpretation of the ramp analysis presented herein.

5.4. Comparison indicators

The comparison of the two architectures is based on four metrics: (i) the overall efficiency η and the performance ratio PR, calculated using equations (18) through (20); and (ii) the volume of water pumped per day, integrated over all irradiance sequences at each site.

6. Results

This section presents the simulation results obtained using the program described in Section 4, applied to the four study sites (Meskine, Agola, Mbé, Soa) over a full year, for both the DC architecture (direct coupling, without an intermediate DC/DC converter) and the AC architecture (DC/DC converter with MPPT, inverter/frequency converter, and modeled in quasi-steady-state conditions).

6.1. Climatic context of the four sites

Figure 5 shows, for each site, the average monthly global irradiance and the average ambient temperature. Meskine and Agola exhibit very similar profiles, with high irradiance during the dry season (DeceMbér–March, ≈290–310 W/m²) that drops sharply during the rainy season (June–August, ≈200–225 W/m²) and a temperature peak in April (34–38 °C), characteristic of the Sudano-Sahelian climate of the Far North and the North. Mbé follows a similar but less pronounced pattern (peak temperature ≈30 °C). Soa is distinguished by consistently lower irradiance (160–280 W/m²) and a moderate, stable ambient temperature (20–25 °C year-round), indicative of a cooler, cloudier high-altitude location.

Figure 5 provides the explanatory framework for the following results: the months of the dry season, characterized by high irradiance and moderate temperatures, are those in which both system configurations approach the us to their nominal capacity, whereas the months of the rainy season, characterized by low and variable irradiance, are those in which the difference between direct DC coupling and AC conversion via MPPT is most pronounced.

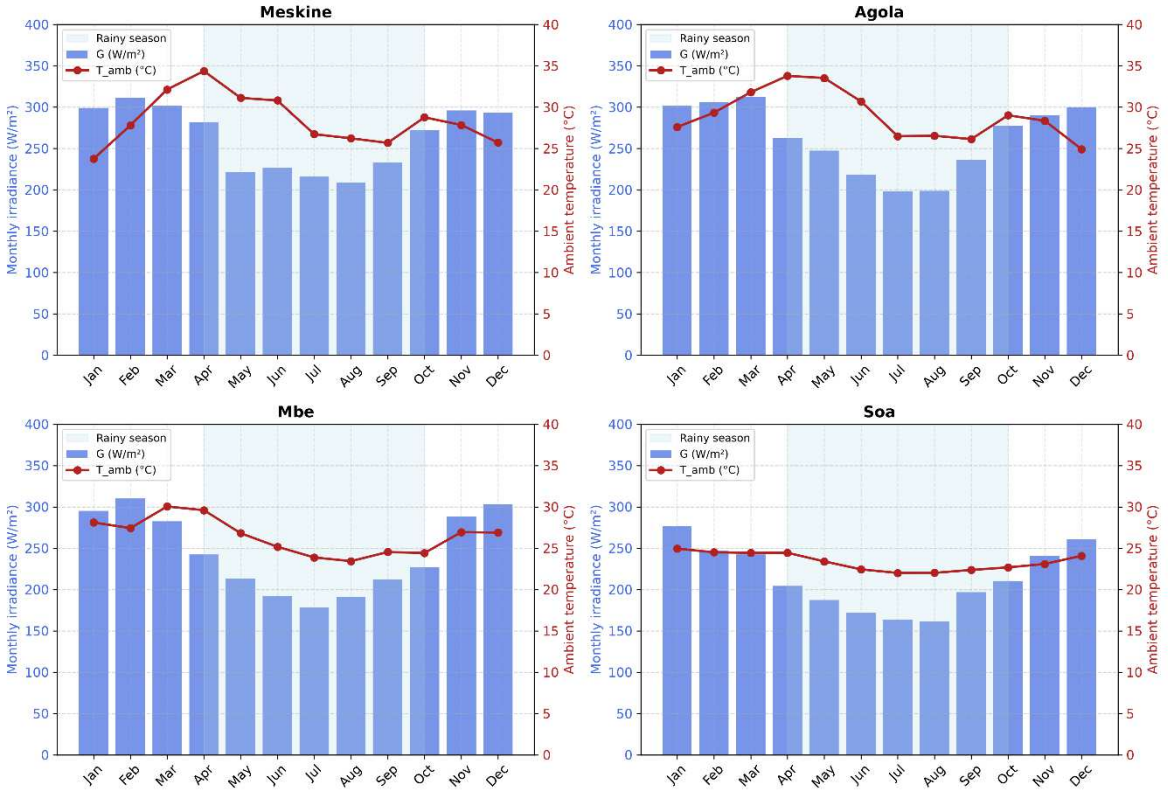


Figure 5: *Monthly climatic conditions (irradiance and temperature).*

6.2. Monthly and annual volume of water pumped

Figure 6 compares, month by month, the volume pumped by each system with water demand. Shortfalls are concentrated during the low-irradiance season: in Meskine, they extend from March through SepteMbér (peaking in April); in Agola, from January through NoveMbér (peaking at 796 m^3 in April for the AC system); in Mbé, an unusual peak occurs in July (617 m^3); in Soa, a deficit is recorded almost every month, including during the dry season, with an extreme maximum of 931 m^3 in August. At the first three sites, the AC line almost consistently exceeds the DC line, confirming that the MPPT makes better use of the resource, particularly during months with low or variable irradiance. In Soa, the two lines are virtually indistinguishable, and the AC even becomes slightly lower than the DC at times starting in May. With the single value of 49 m^3 per day applied to the four sites, the comparative analysis amounts to evaluating, for the same system design and the same reference demand, the actual pumping capacity achieved under each site's specific climate, and verifying whether this capacity is sufficient to meet the demand. For Meskine, the results indicate that the DC covers only 83% of annual demand (14,900 m^3 out of 17,885 m^3), whereas the AC achieves 99 % (17,700 m^3), representing near-complete coverage. None of the four sites fully covers the reference demand, with coverage rates ranging from 75% (Soa-AC) to 99% (Meskine-AC). This situation reflects the methodological choice of a single demand value (49 m^3/day) applied to all sites to ensure climatic comparability; in a real-world design, the peak power of the array would be adjusted site by site to ensure full coverage. The observed DC/AC performance difference can be attributed solely to the solar and thermal climate of each site.

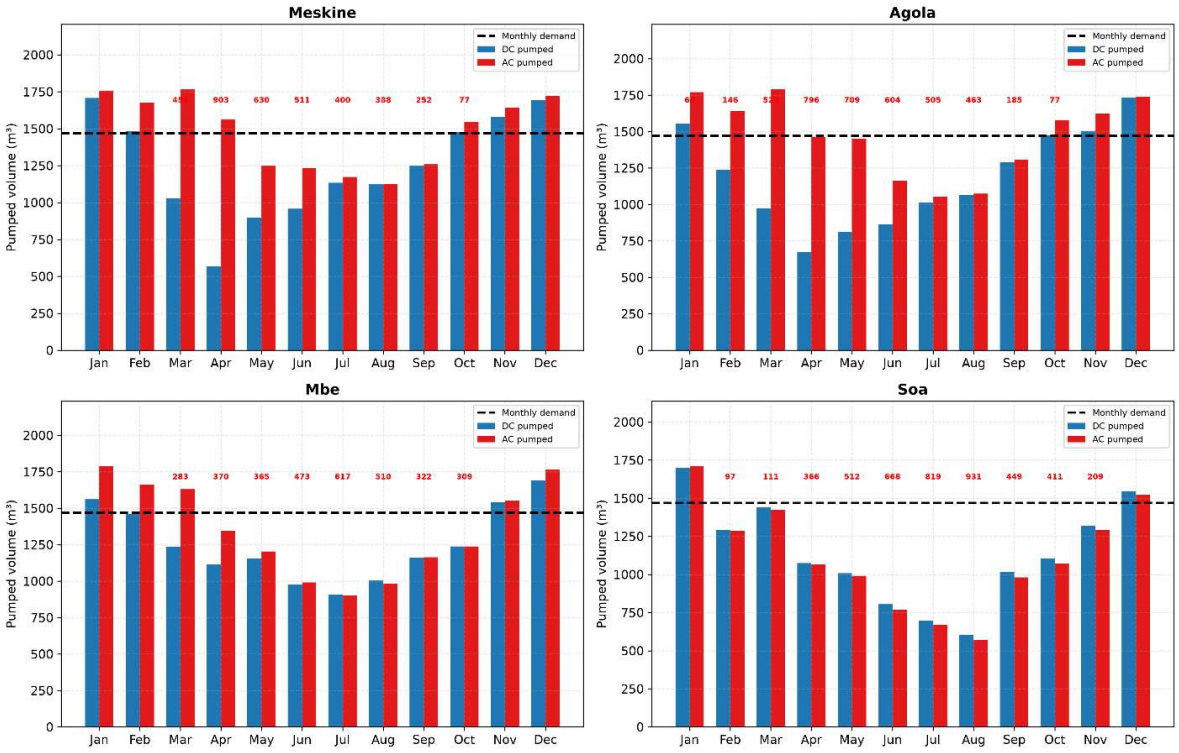


Figure 6: *Monthly pumped volume (DC vs. AC) and demand.*

Figure 7 aggregates these volumes over the entire year and shows the relative increase in AC/DC: Meskine (DC ≈ 14,900 m^3/year, AC ≈ 17,700 m^3/year, +18.9%), Agola (DC ≈ 14,200 m^3/year, AC ≈ 17,650 m^3/year, +24.3%, the highest increase in the study), Mbé (DC ≈ 15,100 m^3/year, AC ≈ 16,250 m^3/year, +7.8%) and Soa (DC ≈ 13,600 m^3/year, AC ≈ 13,350 m^3/year, −1.8%, the only site where AC overall pumps less than DC over the course of the year). This ranking (Agola > Meskine > Mbé > Soa) is directly correlated with the climate profile of each site (Figure 5): within the four simulated sites, the largest AC gains were observed under the higher-irradiance conditions represented by Agola and Meskine. This result is consistent with the orders of magnitude reported by Deli et al. [29], which show that an incremental-conductance MPPT can increase the pumped volume by a factor of 3 to 10 compared to direct coupling in the Sudano-Sahelian zone of Cameroon. The more moderate difference observed here can be explained by lower HMT conditions (38 m vs. 24–60 m) and by the fact that the comparison involves two complete architectures, rather than the same DC coupling with or without MPPT. This result also confirms the trend reported by Meunier et al. [7] for isolated rural communities, where the AC architecture with MPPT is also preferred for deep wells and sites with high irradiance variability.

In Soa, the combination of lower irradiance and moderate temperatures reduces the margin for improvement that can be achieved through power electronics, while losses inherent to the AC conversion chain become proportionally more significant. This inversion, at -1.8%, is consistent with the observations of Chandel et al. [15], who note that the MPPT gain deviates marginally when irradiance is low and relatively stable, and that AC conversion losses then become predominant. This result is also consistent with the conclusion reached by Elgendy et al. [22], who show that constant-voltage control can offer an attractive compromise compared to conventional MPPT algorithms in certain low-irradiance operating ranges.

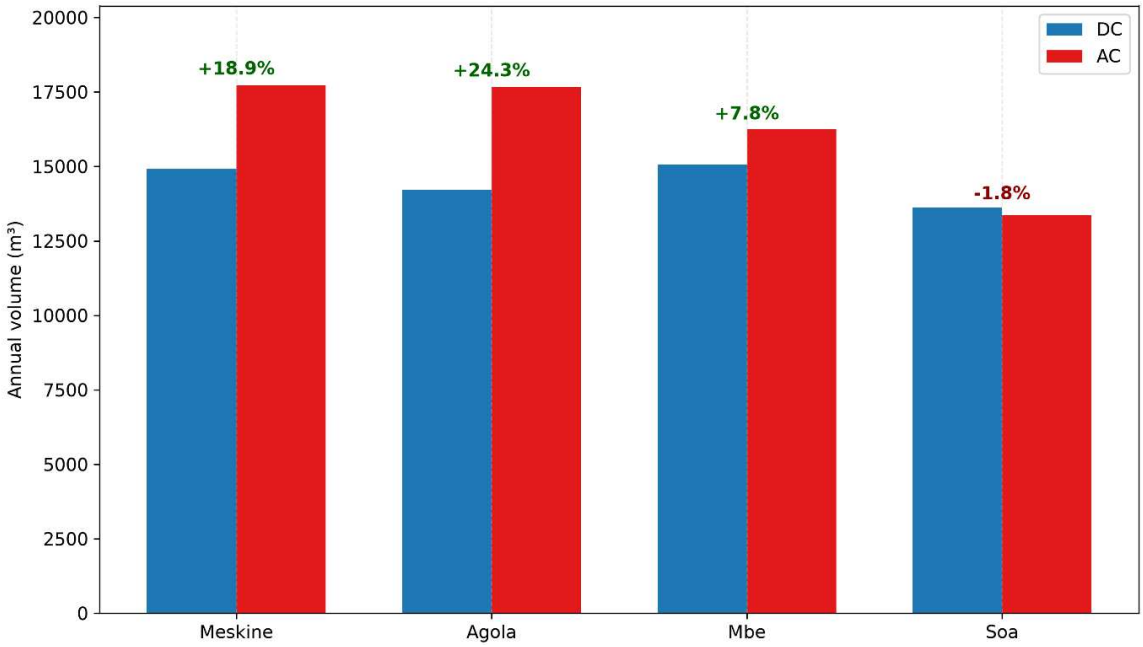


Figure 7: *Annual volume pumped per site (DC vs. AC).*

6.3. Monthly overall energy efficiency

Figure 8 shows the overall monthly energy efficiency ($\eta = E_{hyd}/E_{PV}$). For Meskine, Agola, and Mbé, this efficiency ranges from 20% to 45%, with a pronounced low in March–April for DC (as low as 16% for Meskine), and the AC curve remains almost continuously above the DC curve, with the difference being greatest during the transitional months. For Soa, the trend gradually reverses starting in April: the DC curve rises above the AC curve and remains there until DeceMbér, consistent with the negative annual gain observed in Figure 7.

The simulated overall yields (20–45%) are consistent with the values reported in the literature for small-scale PV pumping systems. Muhsen et al. [27] report typical overall efficiencies of 3–10% in the Sahel region with high HMT, while Meunier et al. [7], obtain efficiencies of 25–40% for optimized systems in Kenya. The discrepancy observed here can be explained by a moderate HMT (38 m) and a PV system that is slightly oversized relative to the pump's power. The AC > DC ranking at sites with high solar radiation is consistent with the conclusions of Bouchakour et al. [21], who show that an asynchronous motor-driven system achieves the best overall efficiency among three compared motor types (DC, asynchronous, and permanent-magnet synchronous) when a sliding-mode control is applied to the inverter. This result is also consistent with the observations of Betka and Moussi [14], who had previously established the energy efficiency superiority of the induction motor architecture for high-power PV pumping applications.

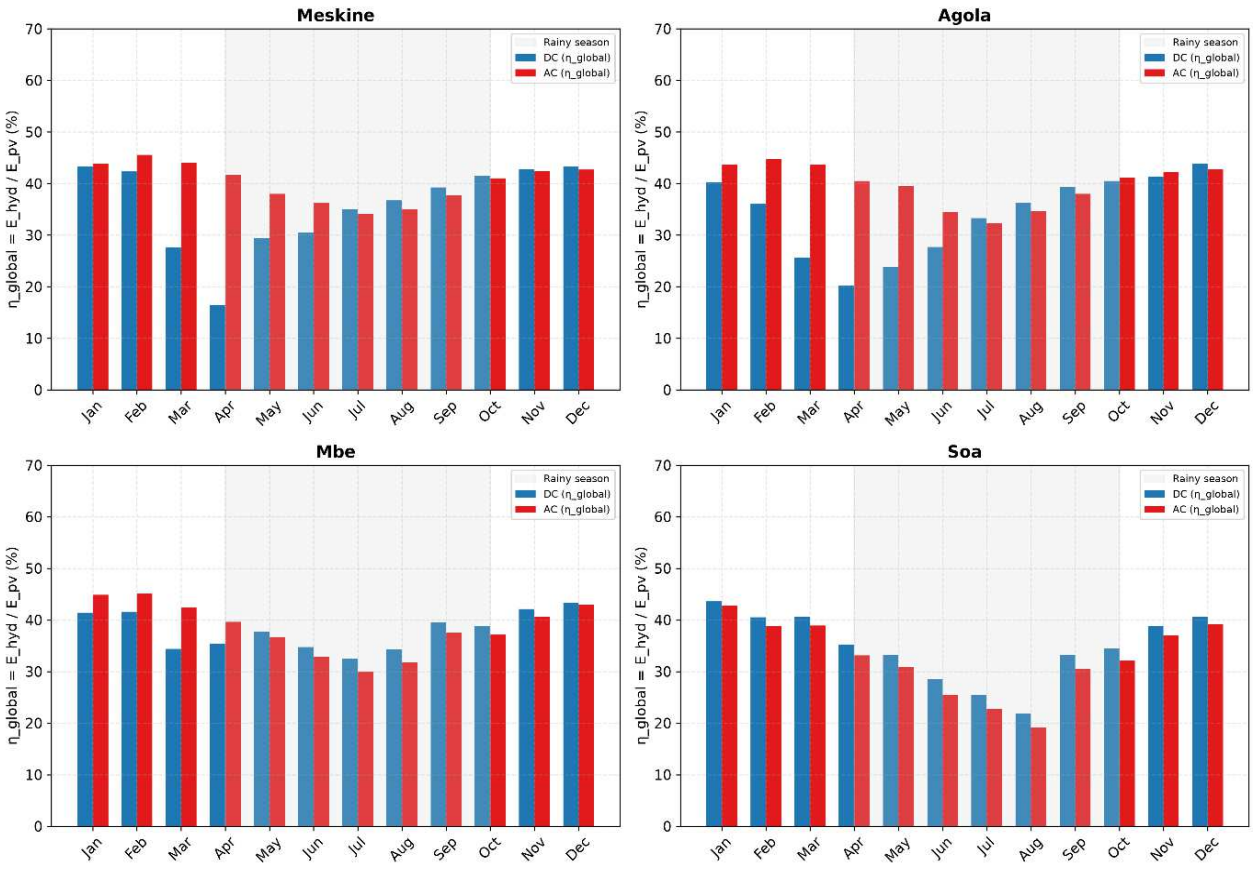


Figure 8 : *Overall energy efficiency (η).*

6.4. Simple and temperature-corrected Performance Ratio

Figure 9 distinguishes between the simple Performance Ratio (referenced to STC conditions) and the temperature-corrected PR (PR_T), which neutralizes the effect of cell temperature. The values obtained are: Meskine (PR DC ≈ 60%, AC ≈ 63%; PR_T DC ≈ 62–63%, AC ≈ 67%), Agola (DC ≈ 60%, AC ≈ 64%; PR_T DC ≈ 63%, AC ≈ 67–68%), Mbé (DC ≈ 61%, AC ≈ 65%; PR_T DC ≈ 64%, AC ≈ 68%), and Soa, which was significantly higher than the other three sites (PR DC ≈ 69%, AC ≈ 72%; PR_T DC ≈ 70.5%, AC ≈ 73.5%), with the lowest DC/AC ratio in the study. The simulated PR values (60–72%) are consistent with values reported for PV installations in tropical climates. Atsu et al. [51] report PR of 70–80% for c-Si modules in sub-Saharan Africa after 12 years. Aboagye et al. [52] obtain similar values in Ghana. The higher PR in Soa (≈ 69–72%) despite lower irradiance can be explained by moderate ambient temperatures (20–25 °C), which limit thermal losses from the cells in high-altitude tropical climates [53, 54].

Since the corrected PR is consistently higher than the simple PR for all sites, the depressive effect of tropical ambient temperatures on the instantaneous power output of the modules is confirmed. Jordan et Kurtz [50] report a typical thermal degradation of 0.4 to 0.5%/°C for crystalline silicon, and Luo et al. [55] confirm this order of magnitude for modules in a humid tropical climate. Soa's significantly better performance, despite lower irradiance, can be explained by its moderate temperatures, which limit thermal losses in the cells, though this is not sufficient to make the AC architecture more advantageous in terms of water volume at this site.

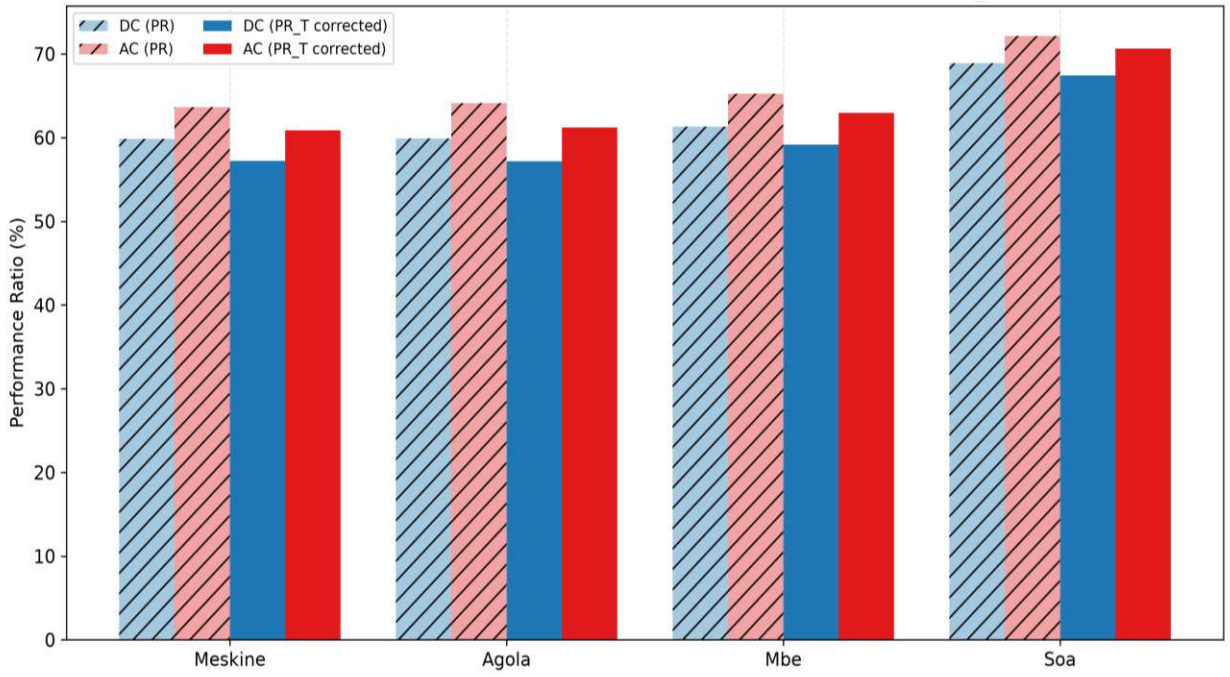


Figure 9: *Simple Performance Ratio (PR) vs temperature-corrected Performance Ratio (PR_T).*

6.5. Operating time and availability

Figure 10 combines the cumulative annual operating time of the motor pump with the system's availability. For Meskine, Agola, and Mbé, the AC operating time (≈2,080–2,260 h) consistently exceeds that of the DC (≈2,060–2,155 h), with a difference that varies significantly: +105 h in Meskine, +154 h in Agola, but only +18 h in Mbé. This difference does not mean that MPPT physically lowers the pump's start-up threshold—which remains a mechanical and hydraulic characteristic—but rather that the MPPT algorithm allows the power threshold required by the motor-pump to be reached sooner by making better use of the available PV power at low irradiance. This behavior is consistent with the observations of Elgendy et al. [16], who show that the effective operating threshold of a pumping system equipped with an MPPT depends on the interaction between the tracking algorithm and the pump's characteristics, as the P&O algorithm can exhibit a significant convergence delay at low irradiance. For Soa, the trend is reversed (DC ≈ 1,800 h > AC ≈ 1,730 h). Availability remains between 20% and 27% across all sites (ranking: Meskine ≈ Agola > Mbé > Soa), with a DC/AC difference of less than 1 point for a given site; overall availability thus appears to be driven more by local solar resources than by the choice of architecture.

The simulated operating times (2,050–2,250 h/year for AC) are consistent with the values reported by Mokeddem et al. [12] for directly coupled systems (2,000–2,300 h/year depending on the HMT), and by Sontake et al. [13] for experimental systems in India. An availability of 20–27% is typical for PV pumping systems without battery storage, where operation is limited to the daily range of usable sunlight.

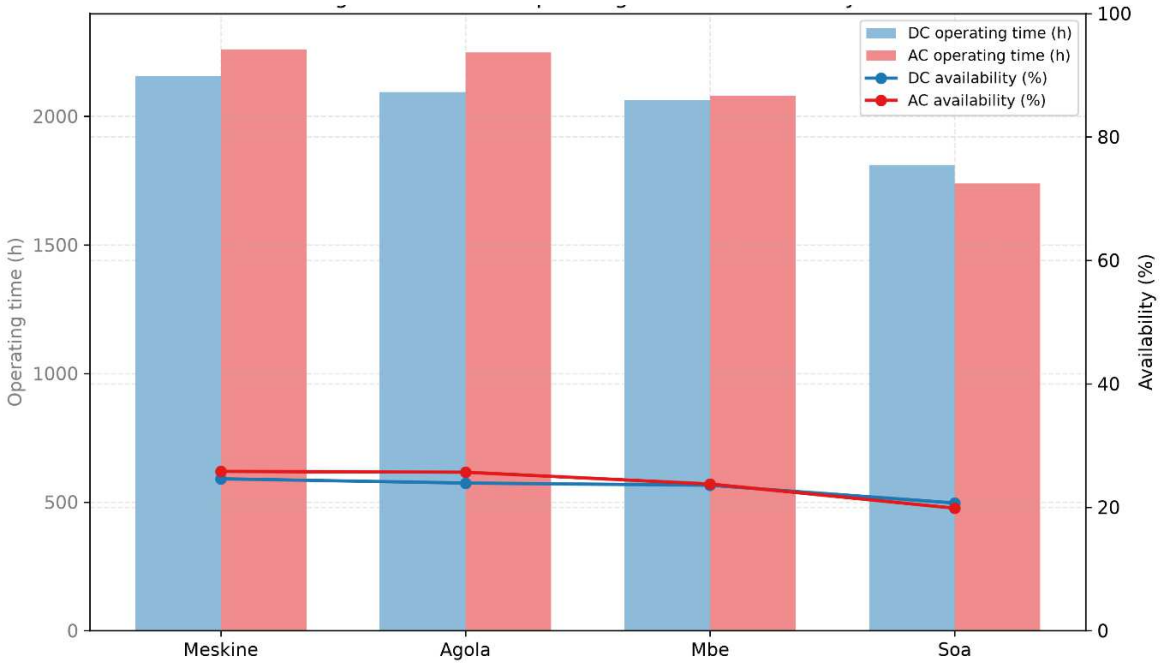


Figure 10: *Annual operating time and availability (utilization rate).*

6.6. Multi-criteria analysis by site

The multi-criteria approach adopted here is inspired by the methodology of Muhsen et al. [27], who recommend evaluating PV pumping systems based on several complementary indicators (volume, efficiency, reliability) rather than a single criterion. It is also consistent with the approach of Schmitter et al. [32] for mapping the suitability of PV pumps in sub-Saharan Africa. Figure 11 summarizes, in the form of two comparable radar charts, four normalized indicators: the radar chart on the left groups the four sites for the DC architecture, while the one on the right groups them for the AC architecture. A comparison of the two radar charts shows that, for Meskine, Agola, and Mbé, the AC envelopes almost entirely encompass the DC envelopes, with a particularly marked difference on the “pumped volume” axis. For Soa, the two envelopes are nearly superimposed in both radar charts, with a slight advantage for DC on the “efficiency” and “availability” axes. This two-block visual structure confirms the study’s central conclusion: the suitability of the AC architecture with MPPT depends heavily on the local climate context.

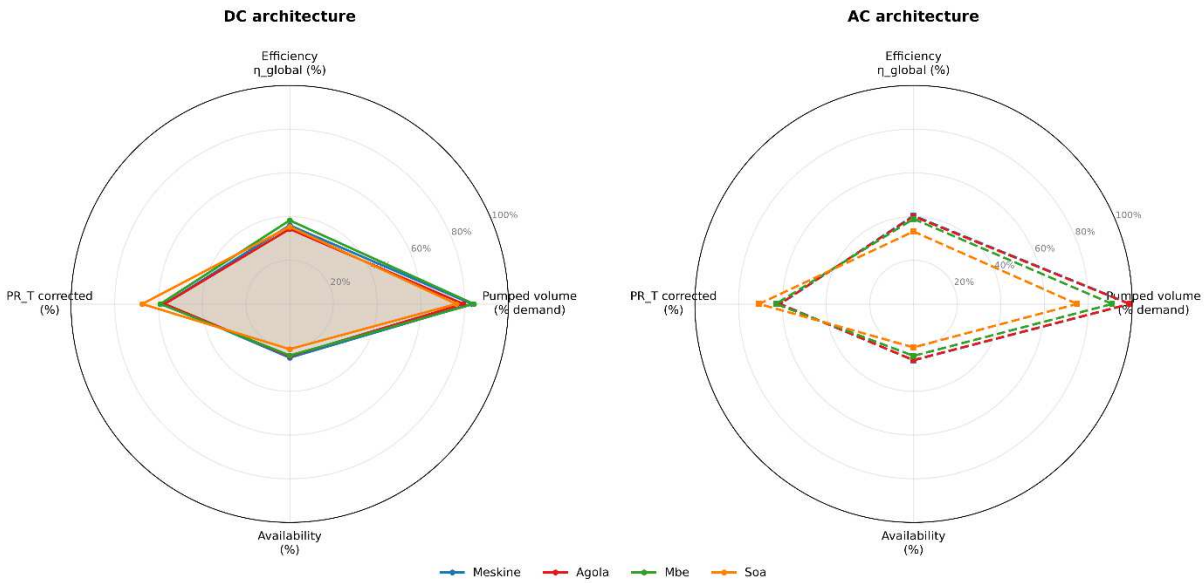


Figure 11 : *Multi-criteria comparison by architecture and by site. Four-axis radar chart (pumped volume as a % of demand, overall efficiency η_{global}, temperature-corrected PR (PR_T), availability).*

6.7. Daily dynamics (Meskine site) and production shortfall

6.7.1 Typical Days

Figure 12 illustrates the performance of the two architectures over three typical days at the Meskine site (clear, average, cloudy), selected according to the characterization approach for PV [58, 45]. On a clear day, AC power slightly exceeds DC power during the midday steady-state period, and AC flow rate reaches its maximum level more quickly and remains there longer; on an average day, the two curves are virtually indistinguishable. On a cloudy day, AC power closely follows increases in irradiance, while DC power exhibits a response of lesser amplitude during rapid transients—a behavior consistent with the advantage of MPPT tracking over direct coupling under variable irradiance conditions, as previously reported in the literature by Ref. [59]. The reservoir charge deviation, represented by the hourly min-max envelope and its average, directly reflects these differences: on a clear day, the SOC oscillates between ≈35% and 100% with nearly identical trajectories across architectures; on an average day, it drops to ≈5% before rising again to ≈80%, with the AC system maintaining a slightly higher SOC during the morning recharge phase; finally, on a cloudy day, the SOC remains confined between 0 and ≈25%, regardless of the system architecture; this recurring daily deficit is the direct cause of the annual deficit reported in Section 6.2 for this site.

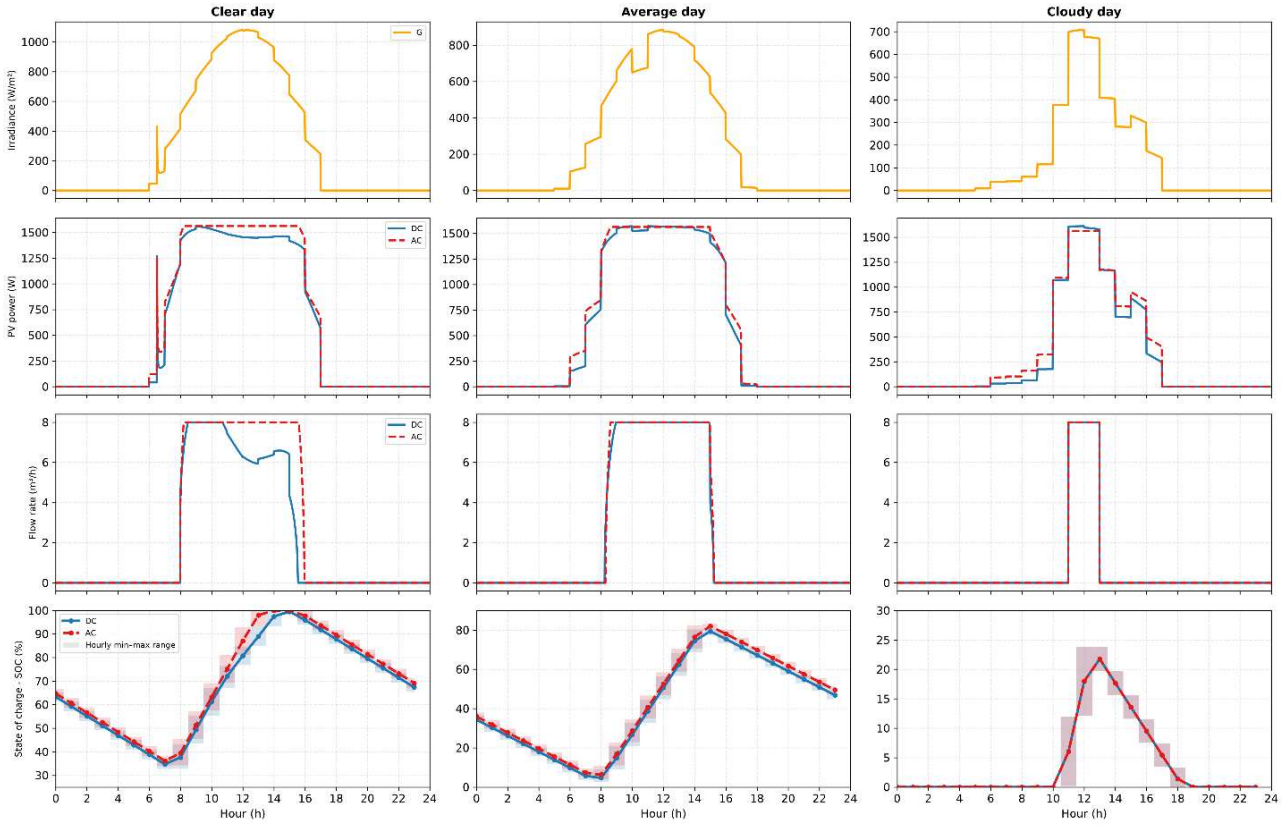


Figure 12: Typical days at the Meskine site: comparison of DC and AC architectures over three representative days (clear, average, cloudy). From top to bottom: irradiance in the plane of the modules G (W/m^2), instantaneous photovoltaic power P_{PV} (W), pumped flow rate Q (m^3/h) and status of charge of reservoir SOC (%). For G, the same irradiance is used for both architectures. For P_{PV}, Q and SOC, the curves are plotted separately. In the panel SOC, the translucent band represents the hourly min-max range of SOC, and the thick line with markers indicates the hourly average. The days were selected based on percentile criteria for average daily irradiance: the 95th percentile (clear, median [average] value), and the 5th percentile (cloudy).

6.7.2 Volume deficit after irradiance ramps

A volume deficit indicator is calculated for each irradiance ramp detected based on the following criterion: an increase in G of at least 200 W/m^2 within 10 minutes or less, followed by a 5-minute period of stability. This criterion is applied independently to each architecture (a ramp is considered only if the flow rate exhibits a jump $\Delta Q \geq 0.1\ m^3/h$), which explains the slight discrepancies in measurements between DC and AC, for example, 153 vs. 148 at Meskine. The volume deficit after the ramp is calculated using Equation (23), which quantifies the volume of water not pumped during the 30 minutes following the start of the ramp, relative to an ideal scenario in which the pump would instantly reach its steady-state flow rate. This formulation is proposed in the present study.

$$\Delta V_{ramp} = \sum_{k=t_{start}}^{t_{start}+30} \left[Q_{plateau} - Q(k) \right] \cdot \Delta t \qquad (23)$$

Where $Q_{plateau}$ is the average flow rate over the 10 minutes following the end of the ramp, $Q(k)$ is the instantaneous flow rate, and $\Delta t = 1/60\ h$.

Table 6 summarizes the cumulative results for the year; Figures S2 and S3 (Supplementary Materials) provide a summary and a statistical distribution.

Table 6: *Cumulative volume deficit following irradiance ramps.*

Site	Architecture	Number of ramps	Total deficit (m^3/year)	Average deficit (L/ramp)	Ratio to annual volume (%)
Agola	DC	191	99.0	518	0.697
	AC	179	96.2	537	0.545
Mbé	DC	213	110.5	519	0.734
	AC	195	106.8	548	0.658
Meskine	DC	153	84.9	555	0.570
	AC	148	84.7	572	0.478
Soa	DC	268	143.9	537	1.057
	AC	249	142.3	572	1.065

Three observations emerge from Table 6. (i) The absolute deficit is similar between the two architectures at all sites (difference < 3.5%): the volume lost during ramp-up is virtually identical regardless of the conversion chain. (ii) The relative deficit is lower for AC at the three sites with high solar radiation (0.08 to 0.15 percentage points), not because of faster recovery but because of a higher annual volume that dilutes the deficit. (iii) In Soa, the AC ratio (1.065%) is slightly higher than the DC ratio (1.057%), confirming that the AC advantage diminishes at low irradiance.

The gain of +18 to +24% at sites with high solar irradiance (Figure 7) suggests that the MPPT's more efficient utilization of PV power contributes more to the AC gain than the restart dynamics, at the considered 1-minute time resolution, without prejudging sub-minute behavior. This result is consistent with Simpson et Marchi [43], who show that the affinity laws of centrifugal pumps impose an inherently slow dynamic response. To our knowledge, few studies have quantified such an irradiance ramp deficit for PV pumping systems: this analysis constitutes an original methodological contribution.

6.8. Gain decomposition of the AC architecture

The ideal MPPT gain is evaluated by assuming the same array powering the same DC motor pump, but equipped with a perfect MPPT: unit tracking efficiency, with no threshold or power limitation. At each time step, the maximum available power is calculated and then converted into flow rate using the same law as the DC branch. This scenario isolates the theoretical contribution of the MPPT, though it does not correspond to a physically feasible configuration. The capture rate is the ratio of the actual AC gain to the ideal MPPT gain. Figure 13 breaks down the annual gain in pumped volume from the AC system relative to the DC system by isolating the contribution of an ideal MPPT applied to the same DC coupling (MPPT gain) from the net gain actually obtained by the full AC system (actual AC gain). The results show that: Meskine (ideal MPPT gain +22.6%, actual AC gain +18.9%, or ≈ 84% of the captured potential); Agola (+27.9% ideal, +24.3% actual, ≈ 87% captured, the highest theoretical added value of the MPPT); Mbé (ideal +11.8%, actual +7.8%, ≈66% captured); Soa (ideal +4.3% only, but actual −1.8%: even the theoretical potential of MPPT is low there, and the intrinsic AC conversion losses alone are sufficient to cancel out and then reverse the

potential gain). This breakdown provides a clear decision-making framework: MPPT-based AC systems are all the more justified when the site exhibits high irradiance variability and/or high ambient temperatures (Agola, Meskine); in a milder and more stable climate (Soa), the additional cost of a frequency converter is not offset by a sufficient increase in output, and the direct-coupled DC architecture becomes technically preferable.

The MPPT potential capture rate is 84–87% at high-irradiance sites (Meskine, Agola), 66% at Mbé, and negligible (< 0%) at Soa. There are consistent with the values reported by Eltawil and Zhao [42]; they note that P&O algorithms typically achieve 85–95% of the theoretical potential under steady-state conditions, but only 60–80% under rapidly varying irradiance. Ebrahim et al. [18] achieve additional gains of 5–10% with PI/FOPI controllers compared to conventional P&O, suggesting a residual margin for improvement for the AC architecture simulated in our work. The fact that the AC gain stems primarily from MPPT, rather than from superior restart dynamics, is consistent with the findings of Bouchakour et al. [21] and those of Saady et al. [19], who attribute most of the gain to better utilization of available PV power rather than to an inherently superior dynamic response. This finding is also consistent with the observations of Vinoth and Singaravelu [20], who show that the superiority of intelligent approaches (ANN, fuzzy logic) over classical P&O is primarily evident in terms of MPP stability and accuracy, rather than response speed.

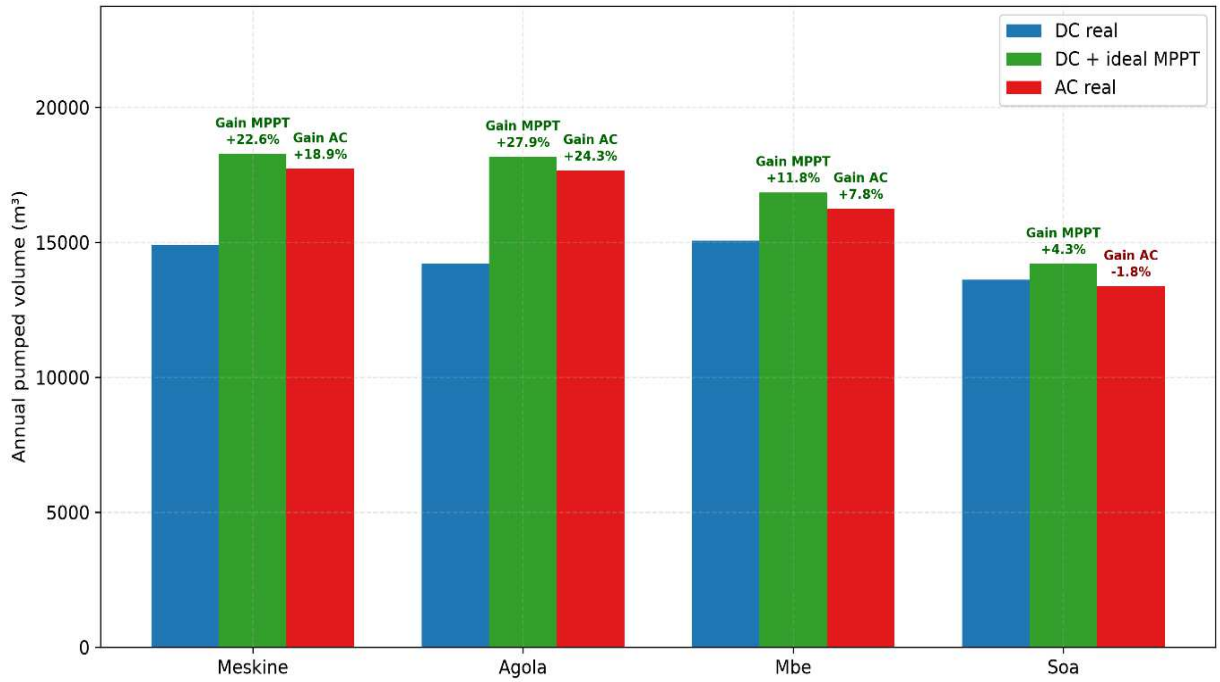


Figure 13: *Breakdown of the AC Architecture's Gain.*

This study focuses on the technical and hydraulic comparison of DC and AC architectures. Technical-economic (LCOW), reliability (LWSP), carbon footprint, and aging analyses are performed using the same simulation framework but will be reported in future work in order to keep this contribution focused on performance comparison.

6.9. Comparative summary of the four sites

Tables 7 to 10 summarize the quantitative data from Figures 5 through 13; the values are approximate readings taken from the graphs (with an accuracy of about one percentage point or a few tens of m^3) intended to facilitate comparisons across sites.

Table 7: *Summary of annual climate conditions.*

Site / Parameter	**Meskine**	**Agola**	**Mbé**	**Soa**
Annual *G* (W/m²)	≈260	≈260	≈250	≈210
Average ambient temperature (°C)	≈28	≈29	≈26	≈23.5
Max. ambient temperature (°C per month)	34.5 (Apr)	38 (Apr)	30 (Mar–Apr)	25 (Mar/Dec)

Table 8: *Annual pumped volumes and breakdown of AC gain.*

Site / Parameter	**Meskine**	**Agola**	**Mbé**	**Soa**
DC flow (m^3/year)	≈14,900	≈14,200	≈15,100	≈13,600
AC flow (m^3/year)	≈17,700	≈17,650	≈16,250	≈13,350
Real AC Gain (%)	+18.9	+24.3	+7.8	−1.8
Ideal MPPT Gain (%)	+22.6	+27.9	+11.8	+4.3
Capture rate	≈84%	≈87%	≈66%	< 0%

Table 9: *Overall energy efficiency and temperature-corrected Performance Ratio.*

Site / Parameter	**Meskine**	**Agola**	**Mbé**	**Soa**
PR DC (%)	≈60	≈60	≈61	≈69
PR AC (%)	≈63	≈64	≈65	≈72
PR_T DC (%)	≈62–63	≈63	≈64	≈70.5
PR_T AC (%)	≈67	≈67–68	≈68	≈73.5

Table 10: *Availability and operating time.*

Site / Parameter	**Meskine**	**Agola**	**Mbé**	**Soa**
DC operating time (hours/year)	≈2,150	≈2,100	≈2,060	≈1,800
AC operating time (hours/year)	≈2,250	≈2,250	≈2,080	≈1,730
DC availability (%)	≈25	≈24	≈23.6	≈20
AC availability (%)	≈26	≈25.7	≈23.8	≈20

The ranking of sites by increase in pumped volume and by increase in AC system efficiency is exactly the same: Agola > Meskine > Mbé > Soa, and is explained by the climatic gradient shown in Table 7: the higher the average annual irradiance and the more pronounced the ambient temperature (Agola, Meskine), the greater the theoretical MPPT potential and the actual net gain; conversely, the coolest and least sunny site (Soa), which nevertheless exhibits the best PR_T due to lower thermal losses, does not have sufficient MPPT potential to compensate for the fixed losses in the AC conversion chain.

6.10. Discussion

All the results point to a single, consistent conclusion: the superiority of the AC architecture with a frequency converter and integrated MPPT over the direct-coupled DC architecture is not universal, but depends on the local climate conditions. This advantage is greatest at sites with high irradiance coupled with high intraday variability and significant ambient temperatures (Agola, Meskine), where the increase in pumped volume (up to +24.3%), the increase in overall energy efficiency, and improved availability combine to give the AC system a clear advantage across all technical and hydraulic performance indicators considered in this study.

The climate dependence of AC gain observed here (Agola > Meskine > Mbé > Soa) is consistent with the findings of Wazed et al. [26] and Schmitter et al. [32], who emphasize the need for a site-specific assessment before any technological choice is made. It also aligns with the recommendations of Muhsen et al. [27] for sub-Saharan Africa, where the variability of solar resources necessitates tailored sizing strategies. This finding is particularly relevant for the deployment of PV-powered pumping in Central Africa, where region-specific climate variability data remain scarcer than those available for West Africa or Southern Africa [23].

This advantage gradually diminishes for an intermediate site (Mbé, +7.8% gain) and disappears entirely for Soa, where AC losses offset the MPPT gain (a difference of -1.8%, which is not statistically significant). This study thus highlights the importance of a site-specific performance evaluation before selecting any photovoltaic pumping architecture in a tropical context, rather than applying a generic sizing rule.

7. Conclusion

This study compared, through annual simulations with 1-minute time steps, the technical and hydraulic performance of direct-coupled DC photovoltaic pumping architectures and AC architectures with inverters/frequency converters featuring MPPT, at four sites in Cameroon representative of contrasting climatic zones: Meskine, Agola, Mbé, and Soa. The literature review, based on the selected Ref. [1, 27], emphasizes that the choice of technology depends on the climatic context and the system's characteristics. The results of our study quantify this dependence within the framework of the selected simulation assumptions.

In the simulated results, the AC architecture shows an increase in pumped volume of up to +24.3% at sites where the gain from MPPT offsets the additional conversion losses (Agola, Meskine), a moderate gain of +7.8% for an intermediate site (Mbé), and a slight decrease of -1.8% for the coolest and least variable site (Soa). This climate-dependent pattern is reflected in the overall energy yield, the temperature-corrected performance ratio, and the annual operating time, all of which converge toward the same ranking of sites: Agola > Meskine > Mbé > Soa.

Analysis of the production shortfall during irradiance ramps shows that, at a 1-minute time resolution, both architectures exhibit comparable absolute shortfalls. The annual volume gain of the AC architecture at sites with high solar radiation is consistent with better utilization of PV power by the MPPT [42, 18], despite additional conversion losses, rather than with fundamentally superior restart dynamics, which is consistent with the conclusions of Bouchakour et al. [21] and Saady et al. [19]. However, the ratio of the deficit to the annual pumped volume remains lower for the AC system at three out of four sites, confirming the relative advantage of this architecture in tropical climates with high irradiance. In Soa, no gain

is observed (a difference of -1.8%, which is not statistically significant), confirming that the choice of technology depends on the climate.

These results should be interpreted as simulation results dependent on design parameters, irradiance profiles, economic assumptions, and the component models used; they do not constitute a universal experimental demonstration of the superiority of any particular architecture. In particular, the 1-minute temporal resolution used in this study—resulting from an hourly projection onto a minute-grid based on solar geometry—does not allow for the quantification of sub-minute transients, which constitute an explicit limitation of this work.

The scope of this work was limited to a technical and hydraulic comparison of the two architectures. The aspects of hydraulic reliability, technical-economic analysis, and carbon footprint will be the subject of future work. This separation allows the present study to address a single, well-defined question: how do direct-coupled DC and variable-frequency AC architectures compare under identical tropical climatic conditions?

The immediate objectives of this study are to: (i) conduct experimental validation on a pilot test bench in accordance with the measurement principles of the IEC 62253:2011 standard [46], in order to compare the simulation results with the actual behavior of the two architectures; (ii) extend the temporal resolution to sub-minute intervals in order to quantify the rapid transients not resolved by the present simulation; (iii) incorporate the combined effects of the PV module's electrical aging and the choice of architecture over the entire lifetime of the installations; and (iv) extend the analysis to advanced control strategies (sliding mode, fuzzy logic, neural networks) already explored in the literature by Ref. [21, 19, 20], in order to refine site-specific sizing recommendations for the deployment of solar pumped storage in Central Africa.

List of Abbreviations

For the sake of clarity and reproducibility, the list below compiles, in alphabetical order, all abbreviations, acronyms, and initialisms used in this article.

AC: Alternating Current
ANN: Artificial Neural Network
BLDC: Brushless DC Motor
DC: Direct Current
FCFA: CFA franc
FOPI: Fractional-Order PI Controller
HMT: Total head
IEC: International Electrotechnical Commission
INC: Incremental Conductance: an MPPT algorithm cited in the literature review but not implemented in this study
LCOE: Levelized Cost of Energy
LCOW: Levelized Cost of Water
LWSP: Probability of Water Supply Interruption
PWM: Pulse Width Modulation
MPPT: Maximum Power Point Tracking
NOCT: Nominal Operating Cell Temperature

OPEX: Operating Expenses
P&O: Perturb & Observe, an MPPT algorithm
PI: Proportional-Integral (controller)
PMSM: Permanent Magnet Synchronous Motor
PR: Performance Ratio
PV: Photovoltaic
SOC: State of Charge
SPVWPS: Solar Photovoltaic Water Pumping System
STC: Standard Test Conditions
WGS 84: World Geodetic System 1984

Supporting information

Graphical representation of Comparative architectures of direct-coupled DC pumping and variable-frequency AC pumping with inverter/VFD and MPPT. Volume deficit after irradiance ramps (annual cumulative deficit per site, mean deficit per ramp, ratio of deficit to annual pumped volume). Distribution of volume deficit per ramp for DC and AC architectures, across all sites. Tables of program modules and their role in the calculation chain, Electrical parameters of the photovoltaic field (Suniva OPT270-60-4-100 module) under STC, and Conversion parameters, yields and coefficients used in the simulation. Methodological note of justification of the consumption rate.

CRediT authorship contribution statement

Felix Ngangoum Welaji, Ariel Teyou Ngoupo: Conceptualization, Methodology, Software, Writing - original draft, Validation, Project administration. **Bertrant Bodo**: Conceptualization, Methodology, Writing - original draft, Validation, Supervision. **Yaouba, Venant Sorel Chara-Dackou, Charles Bertrand Gubong Takam, Lyse Vanessa Ngansop, Antoine Fanyep Nana, Elie Bertrand Kegne Signe**: Conceptualization, Methodology, Writing - original draft. All authors read and approved the final manuscript.

Ethics approval and consent to participate

Not applicable.

Consent for publication

Not applicable.

Funding

No specific project funding was received for this work.

Data availability

The climate input is based on PVGIS hourly data (Typical Meteorological Year) for Meskine, Agola, Mbé, and Soa, Cameroon, 2005–2023. The simulation scripts and processed result tables can be made available by the corresponding author upon reasonable request.

Declaration of Competing Interest

The authors declare that they have no known competing financial interests or personal relationships that could have appeared to influence the work reported in this paper.

Declaration of generative AI use

During the preparation of this work, the author(s) used ChatGPT and Claude in order to assist with the following tasks: (i) language editing and reformulation of technical passages, and (ii) assistance with the development of Python and Fortran programming scripts used in the simulations. The author(s) also used DeepL for preliminary translation drafts. After using these tools, the author(s) reviewed and edited the content as needed and take(s) full responsibility for the content of the published article.

Competing Interests

The authors declare no competing interests.

Conflict of Interests

The authors declare that there is no conflict of interests regarding the publication of this paper.

Acknowledgements

The authors acknowledge the PVGIS database (European Commission, Joint Research Centre) for the free availability of the Typical Meteorological Year (TMY) data used as input to the simulations.

References

[1] V. C. Sontake and V. R. Kalamkar, "Solar photovoltaic water pumping system — A comprehensive review.," *Renewable and Sustainable Energy Reviews,* vol. 59, p. 1038–1067, 2016.

[2] M. Aliyu, G. Hassan, S. A. Said, M. U. Siddiqui, A. T. Alawami and I. M. Elamin, "A review of solar-powered water pumping systems.," *Renewable and Sustainable Energy Reviews,* vol. 87, p. 61–76, 2018.

[3] C. Gopal, M. Mohanraj, P. Chandramohan and P. Chandrasekar, "Renewable energy source water pumping systems — A literature review.," *Renewable and Sustainable Energy Reviews,* vol. 25, p. 351–370, 2013.

[4] G. Li, Y. Jin, M. W. Akram and X. Chen, "Research and current status of the solar photovoltaic water pumping system — A review.," *Renewable and Sustainable Energy Reviews,* vol. 79, p. 440–458, 2017.

[5] L. Gevorkov, J. L. Domínguez-García and L. T. Romero, "Review on solar photovoltaic-powered pumping systems.," *Energies,* vol. 16, no. 1, p. 94, 2023.

[6] K. Muralidhar and N. Rajasekar, "A review of various components of solar water-pumping system: Configuration, characteristics, and performance," *International Transactions on Electrical Energy Systems,* vol. 31, no. 9, p. e13002, 2021.

[7] S. Meunier, M. Heinrich, L. Quéval, J. A. Cherni, L. Vido, A. Darga, P. Dessante, B. Multon, P. K. Kitanidis and C. Marchand, "A validated model of a photovoltaic water pumping system for off-grid rural communities," *Applied Energy,* vol. 241, pp. 580-591, 2019.

[8] H. M. B. Metwally and W. R. Anis, "Dynamic performance of directly coupled photovoltaic water pumping system using D.C. shunt motor," *Energy Conversion and Management,* vol. 37, no. 9, p. 1407–1416, 1996.

[9] A.-K. Daud and M. M. Mahmoud, " Solar powered induction motor-driven water pump operating on a desert well, simulation and field tests," *Renewable Energy,* vol. 30, no. 5, p. 701–714, 2005.

[10] W. Z. Fam and M. K. Balachander, "Dynamic performance of a DC shunt motor connected to a photovoltaic array," *IEEE Transactions on Energy Conversion,* vol. 3, no. 3, p. 613–617, 1988.

[11] M. Akbaba and M. C. Akbaba, "Dynamic performance of a photovoltaic-boost converter powered DC motor-pump system," in *IEMDC 2001 — IEEE International Electric Machines and Drives Conference*, 2001.

[12] A. Mokeddem, A. Midoun, D. Kadri, S. Hiadsi and I. A. Raja, "Performance of a directly-coupled PV water pumping system," *Energy Conversion and Management,* vol. 52, no. 10, p. 3089–3095, 2011.

[13] V. C. Sontake, A. K. Tiwari and V. R. Kalamkar, "Experimental investigations on the seasonal performance variations of directly coupled solar photovoltaic water pumping system using centrifugal pump," *Environment, Development and Sustainability,* vol. 23, no. 6, p. 8288–8306, 2021.

[14] A. Betka and A. Moussi, "Performance optimization of a photovoltaic induction motor pumping system," *Renewable Energy,* vol. 29, no. 14, p. 2167–2181, 2004.

[15] S. S. Chandel, M. N. Naik and R. Chandel, "Review of performance studies of direct coupled photovoltaic water pumping systems and case study," *Renewable and Sustainable Energy Reviews,* vol. 76, p. 163–175, 2017.

[16] M. A. Elgendy, B. Zahawi and D. J. Atkinson, "Assessment of perturb and observe MPPT algorithm implementation techniques for PV pumping applications," *IEEE Transactions on Sustainable Energy,* vol. 3, no. 1, p. 21–33, 2012.

[17] J. Arfaoui, H. Rezk, M. Al-Dhaifallah, F. Elyes and M. Abdelkader, "Numerical performance evaluation of solar photovoltaic water pumping system under partial shading condition using modern optimization," *Mathematics,* vol. 7, no. 11, p. 1123, 2019.

[18] M. A. Ebrahim, A. Osama and K. M. Kotb, "Real-time dynamic performance enhancement for solar-powered pumping systems using PI-based MPPT techniques," *Journal of Solar Energy Engineering,* vol. 145, no. 6, p. 061001, 2023.

[19] I. Saady, B. Majout, I. El Kafazi, M. Karim, B. Bossoufi, N. El Ouanjli, S. Mahfoud, A. Althobaiti, T. A. H. Alghamdi and M. Alenezi, "Improving photovoltaic water pumping system performance with ANN-based direct torque control using real-time simulation," *Scientific Reports,* vol. 15, p. 4024, 2025.

[20] K. Vinoth Bresnav and S. Singaravelu, "Implementation and dynamic analysis (variations in irradiance) of MPPT control using ANN/Fuzzy Logic/P&O in a PV power system for high power applications," *Discover Electronics,* vol. 3, p. 43, 2026.

[21] A. Bouchakour, M. Brahami and A. Borni, "Comparative Study on Photovoltaic Pumping Systems Driven by Different Motors Optimized with Sliding Mode Control," *International Journal of Engineering and Technology Innovation,* vol. 7, no. 3, p. 201–216, 2017.

[22] M. A. Elgendy, B. Zahawi and D. J. Atkinson, "Comparison of directly connected and constant voltage controlled photovoltaic pumping systems," *IEEE Transactions on Sustainable Energy,* vol. 1, no. 3, p. 184–192, 2010.

[23] I. Neher, S. Crewell, S. Meilinger, U. Pfeifroth and J. Trentmann, "Photovoltaic power potential in West Africa using long-term satellite data," *Atmospheric Chemistry and Physics,* vol. 20, no. 21, p. 12871–12888, 2020.

[24] W. B. Mol, W. H. Knap and C. C. van Heerwaarden, "Reconciling observations of solar irradiance variability with cloud size distributions," *Journal of Geophysical Research: Atmospheres,* vol. 128, no. 7, p. e2022JD037894, 2023.

[25] A. Agüera-Pérez, M. J. Espinosa-Gavira, J. C. Palomares-Salas, J. J. González-de-la-Rosa, J. M. Sierra-Fernández and O. Florencias-Oliveros, "Meteorological contexts in the analysis of cloud-

induced photovoltaic transients: A review," *Renewable and Sustainable Energy Reviews,* vol. 202, p. 114689, 2024.

[26] S. M. Wazed, B. R. Hughes, D. O'Connor and J. K. Calautit, "A review of sustainable solar irrigation systems for Sub-Saharan Africa," *Renewable and Sustainable Energy Reviews,* vol. 81, no. P1, p. 1206–1225, 2018.

[27] D. H. Muhsen, T. Khatib and F. Nagi, "A review of photovoltaic water pumping system designing methods, control strategies and field performance," *Renewable and Sustainable Energy Reviews,* vol. 68, no. P1, p. 70–86, 2017.

[28] E. M. Nfah and J. M. Ngundam, "Feasibility of pico-hydro and photovoltaic hybrid power systems for remote villages in Cameroon," *Renewable Energy,* vol. 34, no. 6, p. 1445–1450, 2009.

[29] K. Deli, E. T. Houdji, N. Djongyang, A. Ayang and J. G. Tamba, "An investigation of incremental conductance based maximum power point tracking for photovoltaic water pumping system performances," *Revue des Energies Renouvelables,* vol. 21, no. 3, p. 455–472, 2018.

[30] K. Deli, E. T. Houdji, A. Ayang, D. K. Kaoga and N. Djongyang, "News models for electrical energy evaluation and water flow rate prediction of the photovoltaic water pumping systems in Cameroon," *International Journal of Engineering and Applied Sciences (IJEAS),* vol. 11, no. 5, pp. 43-55, 2024.

[31] A. F. Tchouli, S. Ngasop Ndiya, H. Tchami, C. B. Nzoundja Fapi and H. Tchakounté, "Optimization of photovoltaic water pumping systems: Progress, limits, and prospects for a healthy energy future," *Journal of Techniques,* vol. 7, no. 1, p. 1–18, 2025.

[32] P. Schmitter, K. S. Kibret, N. Lefore and J. Barron, "Suitability mapping framework for solar photovoltaic pumps for smallholder farmers in sub-Saharan Africa," *Applied Geography,* vol. 94, p. 41–57, 2018.

[33] E. Oppong Danso, C. Dietzen, W. Akortey, B. K. B. Mensah, P. B. Obour, J. B. A. Nyasapoh, E. Agyapong, E. G. Ayayi, N. O. O. Bonsu, M. O. Adu, E. Arthur, J. Ulzen, T. Atta-Darkwa, E. B. Sabi, S. Abenney-Mickson and M. N. Andersen, "Can solar-powered irrigation systems naturally meet crop water requirements? Proof of concept from a case study in Sub-Saharan Africa," *Irrigation and Drainage,* vol. 74, no. 4, p. 1423–1435, 2025.

[34] H. Xie, C. Ringler and M. A. H. Mondal, "Solar or diesel: A comparison of costs for groundwater-fed irrigation in Sub-Saharan Africa under two energy solutions," *Earth's Future,* vol. 9, no. 4, p. e2020EF001611, 2021.

[35] A. N. Tchudjo-Tchuente, J. Ouamba-Fedjo, A. Fopah-Lele and J. G. Tamba, "Evaluating the Levelized Cost of Energy (LCOE) of irrigation systems based on solar PV and diesel generator for a green bean crop in Cameroon," *Energy Strategy Reviews,* vol. 61, p. 101826, 2025.

[36] Y. Gunawan, V. Nurliyanti, N. Akhiriyanto, S. Kasbi, K. Ahadi, Sujono, M. N. M. Rizkillah and M. R. F. Permana, "A Comparative Study of Photovoltaic Water Pumping System-Driving Conventional AC Single-phase and Three-phase Motor Submersible Pumps," *EVERGREEN Joint Journal of Novel Carbon Resource Sciences & Green Asia Strategy,* vol. 9, no. 3, p. 893–902, 2022.

[37] K. Deli, N. Djongyang, D. Njomo and D. Kidmo, "A rainy month performance evaluation of photovoltaic module and performance prediction of the PV water pumping systems under soudano sahelian climate," *International Journal of Electrical Components and Energy Conversion,* vol. 4, no. 1, p. 61–71, 2018.

[38] K. Deli, N. Djongyang, D. Njomo and J. G. Tamba, "Photovoltaic water pumping systems as alternative to gasoline water pumping systems in agriculture in Cameroon: CO2 emissions assessment," *Revue des Energies Renouvelables,* vol. 21, no. 2, pp. 279 - 294, 2018.

[39] W. De Soto, S. A. Klein and W. A. Beckman, "Improvement and validation of a model for photovoltaic array performance," *Solar energy,* vol. 80, no. 1, pp. 78-88, 2006.

[40] J. A. Duffie and W. A. Beckman, Solar Engineering of Thermal Processes, 4th ed. ed., Wiley, 2013.

[41] E. Skoplaki and J. A. Palyvos, "On the temperature dependence of photovoltaic module electrical performance: A review of efficiency/power correlations," *Solar energy,* vol. 83, no. 5, pp. 614-624, 2009.

[42] M. A. Eltawil and Z. Zhao, "MPPT techniques for photovoltaic applications," *Renewable and Sustainable Energy Reviews,* vol. 25, p. 793–813, 2013.

[43] A. R. Simpson and A. Marchi, "Evaluating the approximation of the affinity laws and improving the efficiency estimate for variable speed pumps," *Journal of Hydraulic Engineering,* vol. 139, no. 12, p. 1314–1317, 2013.

[44] J. F. Gülich, Centrifugal Pumps, 2nd ed. ed., Berlin, Heidelberg: Springer, 2010, pp. 665-714.

[45] A. Hadj Arab, F. Chenlo, K. Mukadam and J. Balenzategui, "Performance of PV water pumping systems.," *Renewable energy,* vol. 18, no. 2, pp. 191-204, 1999.

[46] IEC, Photovoltaic pumping systems — Design qualification and performance measurements. , ., vol. IEC 62253:2011, Geneva: International Electrotechnical Commission, 2011.

[47] B. Marion, J. Adelstein, K. Boyle, H. Hayden, B. Hammond, T. Fletcher, B. Canada, D. Narang, D. Shugar, H. Wenger, A. KiMbér, L. Mitchell, G. Rich and T. Townsend, "Performance parameters for grid-connected PV systems," in *Conference Record of the IEEE Photovoltaic Specialists Conference*, 2005.

[48] S. S. Chandel, M. N. Naik and R. Chandel, "Review of solar photovoltaic water pumping system technology for irrigation and community drinking water supplies," *Renewable and Sustainable Energy Reviews,* vol. 49, p. 1084–1099, 2015.

[49] IEC, Rotating electrical machines – Part 1: Rating and performance, Vols. IEC 60034-1:2026, Geneva: International Electrotechnical Commission, 2026.

[50] D. C. Jordan and S. R. Kurtz, "Photovoltaic degradation rates — an analytical review," *Progress in Photovoltaics,* vol. 21, no. 1, p. 12–29, 2013.

[51] D. Atsu, I. Seres, M. Aghaei and I. Farkas, "Analysis of long-term performance and reliability of PV modules under tropical climatic conditions in sub-Saharan," *Renewable Energy,* vol. 162, p. 285–295, 2020.

[52] B. Aboagye, S. Gyamfi, E. A. Ofosu and S. Djordjevic, "Degradation analysis of installed solar photovoltaic (PV) modules under outdoor conditions in Ghana," *Energy Reports,* vol. 7, p. 6921–6931, 2021.

[53] D. A. Quansah and M. S. Adaramola, "Ageing and degradation in solar photovoltaic modules installed in northern Ghana," *Solar Energy,* vol. 173, p. 834–847, 2018.

[54] D. A. Quansah, M. S. Adaramola and G. Takyi, "Solar photovoltaics degradation and impact on techno-economics: A review," *Energy Science & Engineering,,* vol. 8, no. 6, p. 2116–2128, 2020.

[55] W. Luo, Y. S. Khoo, P. Hacke, D. Jordan, L. Zhao, S. Ramakrishna, A. G. Aberle and T. Reindl, "Analysis of the long-term performance degradation of crystalline silicon photovoltaic modules in tropical climates," *IEEE Journal of Photovoltaics,* vol. 9, no. 1, p. 266–271, 2018.

[56] M. I. Islam, M. S. Jadin, A. Al Mansur and T. Alharbi, "Electrical performance and degradation analysis of field-aged PV modules in tropical climates: A comparative experimental study," *Energy Conversion and Management: X,* vol. 24, p. 100719, 2024.

[57] J. Hay and J. Davies, "Calculations of the solar radiation incident on an inclined surface," in *Proceedings of the First Canadian Solar Radiation Data Workshop*, Downsview, Canada, 1980.

[58] IEC 61702:1995, "Rating of direct coupled photovoltaic (PV) pumping systems," International Electrotechnical Commission.

[59] G. El-Saady, E. N. A. Ibrahim and M. Ahmed, "Optimal photovoltaic water pumping system performance under different operating conditions," *JES. Journal of Engineering Sciences,* vol. 43, no. 1, p. 16–32, 2015.

Supplementary Files

This is a list of supplementary files associated with this preprint. Click to download.

- Supplementarymaterial.docx